Study of Dynamics and Nanoscale Heat Transfer of Head Disk Interface in Hard Disk Drives

by

Yuan Ma

A dissertation submitted in partial satisfaction of the

requirements for the degree of

Doctor of Philosophy

In

Engineering – Mechanical Engineering

in the

Graduate Division

of the

University of California, Berkeley

Committee in charge:
Professor David B. Bogy, Chair
Professor Panayiotis Papadopoulos
Professor Jeffrey B. Neaton
Summer 2018

Study of Dynamics and Nanoscale Heat Transfer of Head Disk
Interface in Hard Disk Drives

Abstract

Study of Dynamics and Nanoscale Heat Transfer of Head Disk Interface in Hard Disk Drives

By

Yuan Ma

Doctor of Philosophy in Engineering-Mechanical Engineering

University of California, Berkeley

Professor David B. Bogy, Chair

Since its introduction in 1956, hard disk drives have become one of the dominant products in the industry of data storage. The capacity of the hard disk drives must keep evolving to store the exploding data generated in the era of big data. This demand pushes the development of technologies including heat assisted magnetic recording (HAMR), microwave assisted magnetic recording (MAMR) and bit-patterned media (BPM) to increase the areal density beyond $1Tb/in^2$. In the development of these technologies, it is essential to have a clear understanding of the dynamics and nanoscale heat transfer behavior across the head-disk interface.

In this dissertation, dynamics and nano-scale heat transfer in the head disk interface are discussed. Experimental study of nano-scale heat transfer is conducted with the specifically designed static touchdown experiment. Simulation strategy that incorporates the wave-based phonon conduction theory was also developed.

In the flying condition, correlation between the temperature and head disk spacing was found at both passive flying stage and modulation stage. When the flying height increases due to either disk surface microwaviness or contact induced modulation, head temperature will increase, with a slight time delay, indicating the existence of a cooling effect as the head approaches the disk.

The static touchdown experiment, which decouples the complicated air bearing from the nano-scale interface was further designed and performed. The heat transfer behavior across a closing nano-scale gap between head and disk was observed and measured. Experimental and simulation results showed general agreement with the theoretical predictions of the wave based theory for radiation and phonon conduction. The effect of different factors including humidity, air pressure, lubricant layer and disk substrate in the static touchdown experiment were also studied separately.

Furthermore, the dynamics of HAMR condition was studied with waveguide heads. The laser induced protrusion was found to be around 1~2 nm in height.

The findings of this dissertation could be applied to future HAMR head/media design, and the static touchdown experiment could be potentially improved to be a new approach to measure material conduction coefficient and emissivity with high special resolution.

Table of Contents

List of Figures

List of Abbreviations

ABS	Air bearing surface
AE	Acoustic Emission
AFM	Atomic Force Microscope
BPM	Bit Patterned Media
CML	Computer Mechanics Lab
DLC	Diamond-Like Carbon
EB	Exabytes
FEM	Finite Element Method
FFT	Fast Fourier Transform
HAMR	Heat Assisted Magnetic Recording
HDD	Hard Disk Drive
HDI	Head Disk Interface
HGA	Head Gimbal Assembly
HMS	Head Media Spacing
LDV	Laser Doppler Vibrometer
MAMR	Microwave Assisted Magnetic Recording
MB	Megabytes
NFT	Near Field Transducer
PCB	Printed Curcuit Board
PID	proportional–integral–derivative
PMR	Perpendicular Magnetic Recording
RAMAC	Random Access Method of Accounting and Control
RH	Relative Humidity
SEM	Scanning Electron Microscope
SNR	Signal to Noise Ration
TB	Terabytes
TDP	Touchdown Power
TDS	Touchdown Sensor
TFC	Thermal Flyheight Control
ZB	Zettabytes

Acknowledgements

August 2013 was the time I first arrived at the United States to start my pursuit of doctoral degree at University of California, Berkeley. My life over the last five years has been an exciting adventure and I would like to express my gratefulness to all the people who have supported me throughout the journey.

I would like to first express my sincere gratitude to my advisor Prof. David B. Bogy. This dissertation is only possible because of Prof. Bogy's unconditional encouragement and support. Prof. Bogy has provided me with precious insights and perspectives throughout the whole process. I learned from him that in research, bold assumptions and careful verification are both essential to reveal the facts that are not yet understood. Prof. Bogy's philosophy of life and lab management also influenced me greatly. These knowledges will certainly benefit me greatly in my future career. I could not have imagined having a better advisor and mentor for my Ph.D study.

Besides my advisor, I would like to thank the rest of my dissertation committee: Prof. Papadopoulos and Prof. Neaton. My gratitude also goes to Prof. Steigmann and Prof. Ma for serving on my qualifying exam committee.

Research in HDD is closely related with industry advancement. The experiment design would have been almost impossible without the support from HDD companies. I thank Western Digital Corporation (WDC) for providing important experimental materials and devices. My special thanks go to Dr. Jih-Ping Peng for being the principal investigator and coordinator from WDC. Jih-Ping has been very easygoing and helpful in sharing his expertise in HDD. I would also like to thank CML alumni, Shaomin Xiong and Yung-Kan Chen from WDC for their help in securing experimental materials and valuable discussions.

I thank all my fellow lab mates for the precious discussions and support. When I first came to Berkeley, senior lab members, Shaomin Xiong, Yung-Kan Chen, Alejandro Rodriguez Mendez and Soroush Sarabi provided me with their resourceful solutions and suggestions. Yung-Kan Chen and Shaomin Xiong shared with me their excellent experimental skills and knowledge. I also learned a lot through the discussions with other CML students, Haoyu Wu, Amin Ghafari, Siddhesh Sakhalkar, Yuying Wu and Qilong Cheng. I especially enjoyed sharing my staging and experimental experience with Qilong Cheng.

During the summers in CML, I was fortunate enough to work with several enthusiastic interns in CML: Yirui Zhang, Akhilesh Somani and Nicola Ganter. I thank them for giving me the opportunity to be their mentor.

Life in Berkeley is enjoyable with all my friends: Dongchi Yu, Junwen Zhong, Yuxu Han, Yumeng Zhang, Yuguang Tong, Shengxi Wang Ruonan Liu and Xiaoyue Jiang.

Finally, I thank my parents and my girlfriend Ran Xin for their love and support throughout my life in Berkeley.

This work is supported in full by the Computer Mechanics Laboratory at the University of California, Berkeley.

Chapter 1 Touchdown Characterization with touchdown sensor and electromagnetic signal

In the big data era, the amount of data that we have created is astonishing. By 2016, human beings had generated around 16 zettabytes (ZB, 1 ZB=10^9 TB) of data and according to a prediction by Seagate, this number will reach 163 ZB in another ten years[1]. On one hand, big data could benefit us in every way of life including health care, education, media, Internet of things (IOT), etc. but on the other hand, it is posing a severe challenge on the data storage industry. Hard disk drives, with its advantages in high areal density, reliability and low price, are one of the dominant products for data storage. Currently, hard disk drive manufactures including Western Digital Corporation, Seagate and Toshiba are producing data storage capability on the order of exabytes (EB, 1 EB=10^6 TB) every year and this number is still increasing[1]. To meet this ever increasing demand of data storage, it is essential to keep developing new technologies that could increase the areal density of the hard disk drives [2].

In this chapter, the evolution of hard disk drives and its basic structure is first introduced, followed by a more specific description on thermal fly-height control technology and touchdown sensor. Next, the heat assisted magnetic recording technology and its necessity and challenges are introduced. Finally, the objective and organization of this thesis are listed

1.1 The basic structure of hard disk drives and its evolution

In general, the current hard disk drives are consisted of hard disks with magnetic layers rotating at high speed, read-write heads that fly on both surfaces of each disk and servo controllers that controls the location of the heads on the disk (Fig. 1.1.1). The glass or aluminum alloy disk substrates are covered with lubricant, diamond-like carbon (DLC) overcoat, magnetic layer and inter layers. The lubricant and DLC overcoat protects the head-disk interface (HDI) from contacts that occasionally happens during operation. The disks are installed co-axially on a motor and rotate at velocities ranging from 5000 rpm to 15000 rpm.

Fig. 1.1.1 Structure of a current commercial hard disk drive

The read-write head is manufactured on a slider which is further installed on the head-gimbal assembly (HGA) (Fig. 1.1.2). Multiple sets of HGA are mechanically connected to the servo controller and the servo controller performs accurate track seeking over the hundreds of thousands of tracks on the disk within the time scale of microseconds.

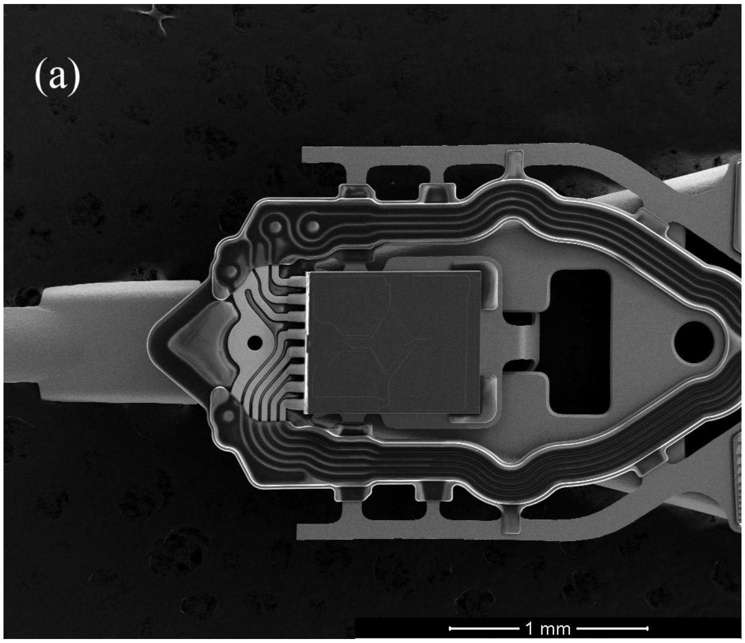

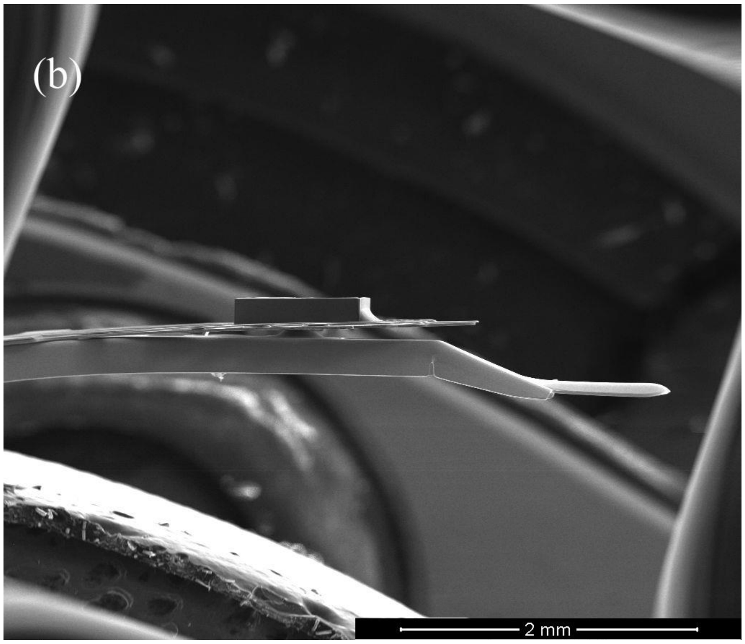

Fig. 1.1.2 HGA under scanning electronic microscope (SEM): (a) top view and (b) side view

On the surface of the slider is the air bearing surface. A unique pattern is etched on this surface to allow the head to stably fly on the disk with specifically defined head disk spacing (Fig. 1.1.3). This pattern also requires the head disk spacing to maintain almost a constant value at different radii on the disk. When the head is flying on the disk, it has a small pitch angle and the minimum head disk spacing point is located at the trailing edge of the slider. In a current perpendicular magnetic recording (PMR) drive, the minimum gap size between the head and disk during passive flying is around 10 nm. This value is further reduced to 1~2 nm during data writing with the thermal fly height control (TFC) technique. This technique will be further described in Section 1.2.

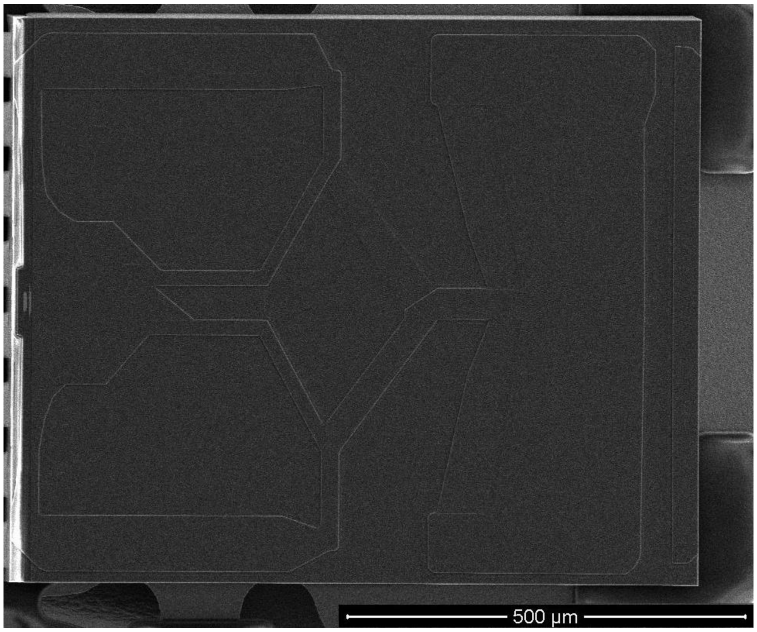

Fig. 1.1.3 Air bearing surface of a PMR head

In a currently available commercial drive, the magnetic bits are arranged perpendicular to the disk plane in the magnetic layer of the disk (Perpendicular Magnetic Recording, PMR). During a writing event, the writer pole located at the center of the trailing edge of the slider flips the bit direction to record either ‘0’ or ‘1’. Similarly, during a reading event, the reader located next to the writer reads the magnetic signal and transfers it to the control circuits on the drive.

Introduced in Sept. 1956, the IBM 305 RAMAC (Random Access Memory Accounting) system was the first hard disk drive (Fig. 1.1.4) [3]. This drive was configured with 50 magnetic disks and rotated at 1,200 rpm. It had a capacity of 5 million characters, which is around 3.75 MB. It used electronic and pneumatic controls for track seeking and the average seeking time are around 600 milliseconds. A small air compressor was used to control the 20 µm air bearing. Self-acting hydrodynamic air bearings, which control the air bearing spacing by forcing ambient air flow through the designed air bearing surface (ABS) on the head, were later introduced in IBM 1301 in 1962, and Winchester in 1973 (Fig. 1.1.5)[4]. The principle of this air bearing control method has been the foundation of today’s hard disk drives.

Fig. 1.1.4 IBM 305 RAMAC [5]

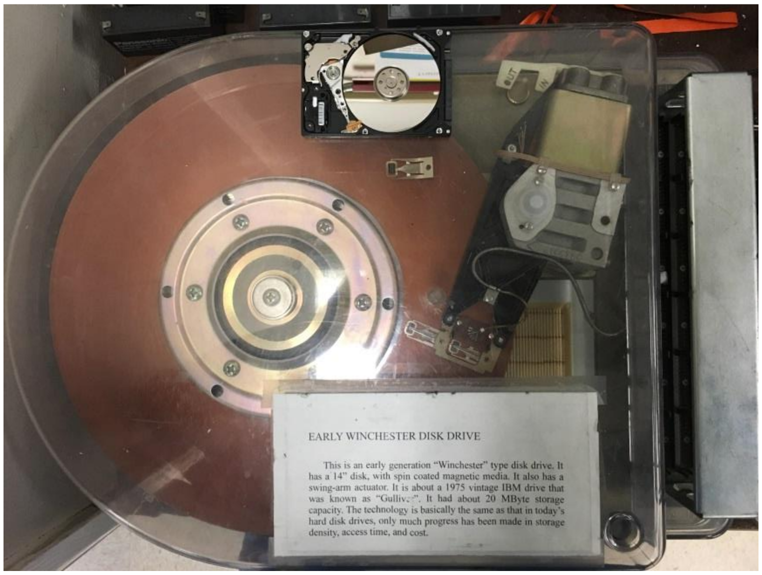

EARLY WINCHESTER DISK DRIVE

This is an early generation "Winchester" type disk drive. It has a 14" disk, with spin coated magnetic media. It also has a swing-arm actuator. It is about a 1975 vintage IBM drive that was known as "Gulliver". It had about 20 MByte storage capacity. The technology is basically the same as that in today's hard disk drives, only much progress has been made in storage density, access time, and cost.

Fig. 1.1.5 Comparison of a Winchester drive, a current 2.5 in hard disk drive, and a read-write head of the Winchester drive

The Winchester drives laid the foundation of air bearing control technique. Since then, technologies in the hard disk drive continues to develop in structure, material and manufacturing: thin film inductive heads and media significantly reduced the size of the head and improved manufacturing efficiency[6, 7]; giant magnetoresistive material (GMR) enabled higher areal density and smaller read transducers [8, 9]; PMR replaced horizontal magnetic recording [10, 11]; thermal fly-height control

(TFC) technique further reduced the head-disk spacing while maintaining the flying stability [12, 13] and helium filled drives enables higher areal density and faster track seeking [14-17].

While these aforementioned technologies have shaped the hard disk drives to what we currently have, more technologies are being developed to further increase the areal density. Shingled magnetic recording (SMR) [18, 19], heat assisted magnetic recording (HAMR) [20], microwave assisted magnetic recording (MAMR) [21, 22], two-dimensional magnetic recording (TDMR) [23-25] and bit-patterned media (BPM) [26-28] are some of the examples.

1.2 The thermal fly-height control technology and touchdown sensor

With higher areal density on the disk, the signal-to-noise ratio (SNR) would decrease unless other dimensions are also reduced. To achieve stable read-write performance, it is necessary to reduce the head- disk clearance. On a Winchester drive, the head disk clearance was 20 μm [4] and this number was decreased to 1/1000 of its original value in the next few decades by altering the ABS design on the head and improving the disk surface quality [11, 29]. While it could be possible to further reduce the head disk spacing down to a couple of nanometers by an improved ABS design, such a small gap over the whole length of the trailing edge would greatly compromise the flying stability and increase the chance of head disk contact [30].

To balance the need of nano-scale head disk clearance and flying stability, thermal fly-height control technology (TFC) was developed [12, 13]. In a TFC slider, a resistive heater element is located inside the head, right above the writer. When supplied with a bias current or voltage, the heater will heat up the local region around it and generate a protrusion on the ABS surface. The protrusion is around 10 μm in diameter and 1~30 nm in height, depending on the power supplied to it. A detailed TFC protrusion shape on a PMR head is measured and simulated in Chapter 4.

Touchdown sensor (TDS, also known as embedded contact sensor, ECS or thermal asperity sensor) is a thin-film resistive sensor that is sensitive to its temperature change [31, 32]. It was first proposed by Shimizu *et al.* for defect mapping on disks. The TDS is located on the surface of the ABS near the writer pole. During the TFC protrusion, it is usually located at the highest protrusion point.

With the combination of TFC and TDS, it is possible to study the thermal-mechanical behavior of the head-disk interface. While the heads used in this paper only have one TFC and one TDS, sliders with double TFC and multiple TDS are under development for future drives.

1.3 Heat assisted magnetic recording and its challenges

As the size of the bits in the current HDDs keeps decreasing, it is facing the super-paramagnetic limit on SNR, stability and writabiligy [20, 33, 34]. All these factors pose an upper limit of areal density achievable by PMR. The areal density of current PMR disks has reached about 1Tb/in^2 and this is believed to be close to the limit. To overcome this limitation and achieve even higher areal density, heat assisted magnetic recording (HAMR) is being developed. During a writing event, HAMR lowers the media coercivity by temporarily heating the media. The magnetic write field needed for data writing after heating can be much lower, which further allows smaller bit size and higher areal density. Locally heating the media is done by applying a laser beam from a laser diode installed on top of the slider. The laser beam travels through a waveguide onto the nearfield transducer (NFT), which is located at the ABS surface and focuses the laser spot size below the diffraction limit.

While HAMR could potentially provide areal density up to 20 Tb/in^2, there still remains many challenges to overcome before the HAMR drives are ready for commercial market. One of the most important issues currently is the reliability of components under high temperature. Failures due to high temperature and contamination on the lubricant, overcoat and substrates have all been observed [35-37].

To address these issues, it is necessary to understand the heat transfer behavior in the nano-scale head disk interface. However, heat transfer through a nano-scale gap is still not fully understood. Theories and experiments have predicted an enhanced heat flux at nano-scale gap [38, 39]. But these theories could not be applied to the head-disk interface directly due to the complicated thermal-mechanical design of the head and disk. Moreover, the dynamics of the HDI adds even more complexity to the problem. Therefore, it is necessary to study the dynamics and heat transfer behavior in the HDI through experimentation and simulation.

1.4 Wave based phonon conduction theory

The wave based phonon conduction theory is based on the extension of Planck’s Law [38-42]. Consider the simple material-gap interface structure shown in Fig. 1.4.1. Assuming the temperatures are different at the two surfaces, the heat flux across the gap can be divided into two portions: radiation and phonon conduction. The radiation heat transfer is based on electromagnetic waves. The distribution of energy transferred is determined by extending the Planck law to non-equilibrium systems that have a net heat flux. The reflection coefficient R can be calculated for any layered structure by known means and the radiation heat flux is governed by the following equation:

$$Q(T_A,T_B) = N\int_0^{\omega_D}\int_0^{\theta_A^*}\left\{(1-|R(\omega,\theta)|^2)\left[P\left(\omega,\theta;T_A,\frac{Q}{Q_A}\right)-P\left(\omega,\theta;T_B,-\frac{Q}{Q_B}\right)\right] - 2|R_A(\omega,\theta)|\sqrt{1-|R(\omega,\theta)|^2}P_{AB}(\omega,\theta;T_A,T_B,Q)\cos\chi\right\}d\Omega$$

where Q is the heat flux, N is the number of polarizations, R is the reflection coefficient, and P is the distribution of emitted energy as a function of angle and frequency of the waves, and χ is a random phase shift. A similar equation holds for phonon conduction, as shown in [42]. For the structure considered here, R is sufficiently small that the last term in the calculations can be ignored. Using this approach, the total heat flux for the structure in Fig. 1.4.1 can be calculated for various materials, temperatures and gap sizes.

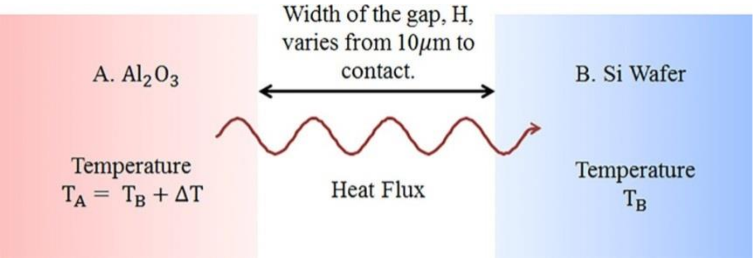

Fig. 1.4.1 Structure of the material-gap interface. The left half space is the hot surface and the right half space is the cold surface.

1.5 Objective of this work

The objective of this work aims to understand the dynamics and nano-scale heat transfer behavior in the head disk interface. Research works are conducted in the following four aspects:

1). Characterize different stages of head-disk interaction at contact proximity and correlate the dynamical response of the head with its temperature change.

2). Experimentally study the nano-scale heat transfer behavior between a head and a static disk under controlled condition and environments.

3). Incorporate wave based phonon conduction theory (the Extension of Planck's law) into a finite element model to simulate the experimental condition and examine the theory.

4). Study the more complicated dynamic response of the wave guide heads.

1.6 Organization of the dissertation

The dissertation is composed of 6 chapters. Chapter 1 offers a brief introduction of the structure and history of hard disk drives, with some emphasis on TFC, TDS and HAMR technology and why it is necessary to study the dynamics and nano-scale heat transfer between the head-disk interface. Chapter 2 discusses the head dynamics and temperature change when flying on a disk at different stages of touchdown and how these two factors are correlated with each other. In Chapter 3, the experimental setup and methodology of the static touchdown experiment are introduced, followed by a detailed discussion on how factors including air, humidity and disk substrates could affect the nano-scale heat transfer behavior. Chapter 4 describes how the wave based phonon conduction theory is incorporated into a finite element analysis model to simulate the static touchdown experiment and how the simulation results are compared with experiments. Chapter 5 presents the dynamic study of wave guide heads. All the experimental and simulation results are concluded in Chapter 6.

Chapter 2 Touchdown Characterization with touchdown sensor and electromagnetic signal

2.1 Introduction

TFC sliders are widely used in current HDDs because of their capability to reduce the local spacing between the head and the disk in a small region around the transducer while maintaining the spacing greater than 10 nm over the rest of the slider [12, 43-46]. With TFC, the flying height of the slider can vary from its designed value to contact. Controlling the flying height of the slider can provide insights into the characteristics of the HDI, especially at contact proximity [43, 47]. At both component level and drive-level, dynamics of thermal protrusion-induced slider-disk contacts have been studied theoretically, experimentally, and by simulations. Acoustic emission (AE) and laser Doppler vibrometer (LDV) measurements are used in component level to observe the slider's dynamics at disk proximity and contact [48-51]. In drive-level testing, on the other hand, the means to evaluate the HDI mainly focus on head-media spacing (HMS) signals, servo control signals and external AE sensors [52, 53].

The recently introduced touchdown sensor (TDS) (also known as an embedded contact sensor or a thermal asperity sensor) has provided another insight to the HDI dynamics. Shimizu *et al.*[31] proposed the embedded contact sensor for defect mapping on disks. This sensor is a thin film element that changes its resistance in proportion to its temperature. Through thermal-mechanical analysis, simulation, and component-level testing, researchers are able to identify different HDI characteristics, including asperities, pits, lube moguls, disk clamping distortions, and surface microwaviness with TDS [54-57]. However, there have been few reports regarding TDS response to HDI spacing and its application in touchdown (TD) stage identification in the drive-level testing. Understanding how the head temperature and head-disk spacing signal are correlated is crucial for the head/media design, tribology design and failure analysis in hard disk drives.

In this chapter, the correlation between the temperature signal from TDS and the spacing signal is experimentally measured at the drive-level and component-level. Different stages of touchdown are further identified in touchdown detection from these signals in both time and frequency domains.

2.2 Experimental setup

2.2.1 Experimental setup for drive-level testing

Drive-level experiments were performed on commercially available PMR hard disk drives operating at 7200 rpm. The test drive is connected to the test computer, which controls the heads to fly on specific tracks and the TFC power supplied to each head. The TDS and HMS signals are obtained from the PCB connection board on the back of the test drive (Fig. 2.2.1). These signals are further acquired by a Lecroy 8620A Oscilloscope.

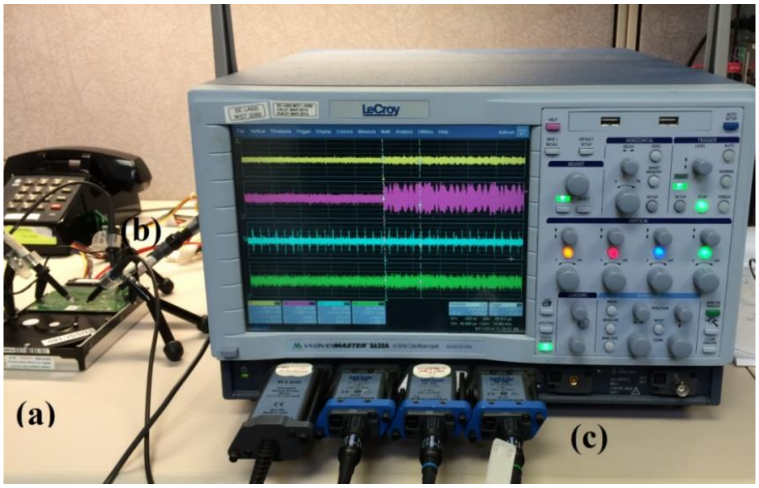

Fig. 2.2.1 Experimental setup containing (a) test drive, (b) test pin and (c) Oscilloscope

Lecroy 8620A is a 4 channel, 6GHz digital oscilloscope that can operate either on standalone mode or controlled by a test computer. In this set of tests, the oscilloscope is controlled by a MATLAB script to acquire index, TDS or magnetic read back signals for further analysis. Due to technical limitations, the TDS and HMS signals were not acquired simultaneously.

2.2.2 Experimental setup for component-level testing

Component-level experiments were performed on a Candela Optical Surface Analyzer (OSA 5100) spin stand. This experimental setup includes LDV, AE and TDS for dynamical and temperature measurement (Fig. 2.2.2).

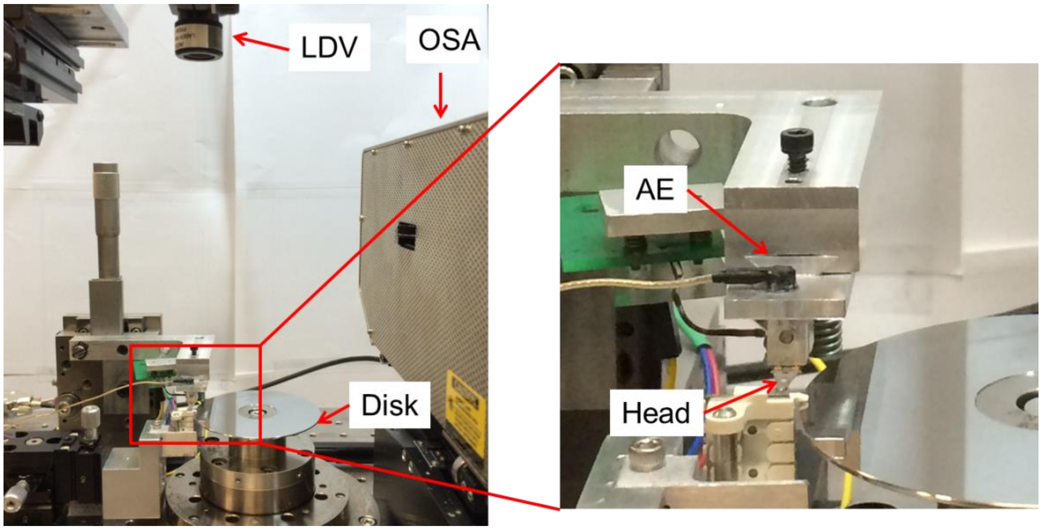

Fig. 2.2.2 Component-level experiment setup

The LDV used in this study was manufactured by Polytech and consists of three components: the main controller (OFV-5000), the interferometer (OPV-512) and the laser probe head (OFV-130). LDV measures vibration by directing a beam of laser onto a reflective surface. The velocity of the test point along the laser beam is calculated from the Doppler shift of the reflected signal. Laser spot size of the LDV differs with different probe head, and the one used in this study has a diameter of 3~4 μm. The output of the LDV is an analog voltage signal, which is proportional to the measured velocity.

The AE sensor is a piezoelectric sensor capable of sensing high frequency (>10 kHz) elastic waves. Since the output level of the sensor is very low, a preamplifier is necessary to amplify the output signal so that it is detectable by the data acquisition system. The AE sensor and preamplifier used in this dissertation is manufactured by Acoustic Emission Technologies (AET).

The data acquisition system on the component-level experimental setup consists of two data acquisition boards manufactured by National Instrument (NI): PCI-6115 and USB-6211. PCI-6115 is a high speed data acquisition board with 4 analog input channels and 2 analog output channels. Its maximum input rate is 4MS/s, enabling it to capture the high frequency signals from LDV, TDS and AE. USB-6211 has a relatively lower input/output ratio and is used to generate the driving voltage for TFC. The wiring diagram of the electrical connection for TFC and TDS are both depicted in Fig. 2.2.3.

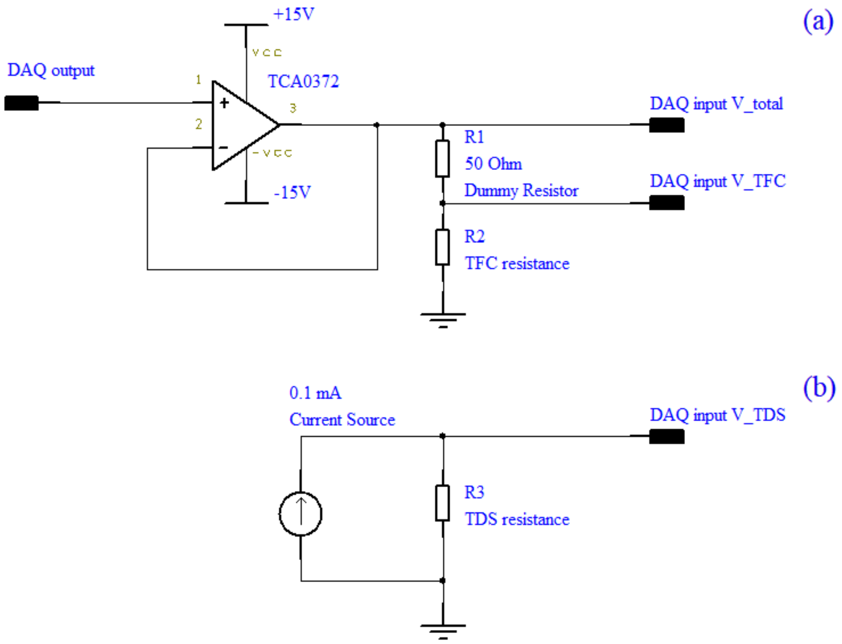

Fig. 2.2.3 Wiring diagram of (a) TFC power supply and (b) TDS power supply.

With the signals acquired from the data acquisition board, the TFC power (P_{TFC}) and TDS resistance can be calculated as below.

$$P_{TFC} = V_{TFC}\left(V_{total} - V_{TFC}\right) / R_{dummy} \tag{2.1}$$

The resistance of the TDS is calculated according to equation 2.2, where I_{cs} is the current provided by the current source. In this set of experiment, the current varies from 0.1 mA to 1mA, depending on specific experiment.

$$R_{TDS} = V_{TDS} / I_{cs} \tag{2.2}$$

2.3 Methodology

To study the dynamics and temperature response of HDI at contact proximity, experiments at drive-level and component-level are both performed. At drive-level, the setup is relatively simpler, but dynamical measurements including AE and LDV are not applicable. Component-level, on the other hand, allows implementation of AE and LDV direct measurements with the price of lower SNR.

2.3.1 TDP measurement

To analyze the TDS signal and its relationship with head disk spacing at different stages of touch down, it is necessary to first determine the touch down power (TDP) of the head on the test track.

At drive-level, TDP was measured through a dithering process. During this process, the TFC power is turned on and off at the first pitch frequency of the ABS (the dithering frequency). The servo position error signal is monitored and transferred to the frequency domain using a Fast Fourier Transform (FFT) in real time. When the dithering frequency peak is observed from the servo position error signal spectrum, the head is considered to be in contact with the disk. The lowest TFC power at which the dithering frequency peak can be observed is defined as the TDP.

At component-level, TDP detection is achieved with the AE sensor. Firstly, the head passively flies on a specific track. The RMS of AE signal at this state is recorded as the AE baseline. Then the TFC power is turned on and increased by 1mW per step (4 revolutions for each step). The RMS of AE is monitored through the process. When it increases beyond 105% of AE baseline, the TFC power of this step is considered to be the TDP.

2.3.2 Head disk spacing measurement

Measuring head disk spacing is achieved with different methods in drive-level and component-level.

At the drive-level, head disk spacing is determined through a combination of the HMS signal, which is calculated from the first and third harmonics of the read back signal by use of the Wallace equation, and touchdown detection [58, 59]. HMS measures the relative fly height variation and touchdown determines the HMS value at which contact happens.

At the component-level, the relative head disk spacing is determined by subtracting the disk profile from the head displacement. Both the disk profile and head displacement are integrated from the LDV velocity signal. To measure head displacement, the LDV laser beam is directed to the back of the slider over the trailing edge center to record the head displacement. For disk profile, the laser beam shines directly on the same track with the slider removed. After integrating these two signals, the disk profile is subtracted from the head displacement to calculate the head disk spacing. touchdown detection is also necessary here to determine contact.

2.3.3 Experimental Scheme

In both drive-level and component-level experiments, the experimental schemes are similar. After detecting the TDP on the specific track, the head first flies passively on this track with TFC power turned off. Then, the TFC power was increased step by step until it reaches 135% of TDP. The spacing signal (either HMS or LDV integrated signal) and TDS data are then recorded in each step for further comparison.

2.4 Results and discussion

2.4.1 Touchdown stage identification

At different levels of TFC power, the HMS and TDS signals showed different patterns (Fig. 2.4.1(a)–(c)). All of the HMS and TDS signals in Fig. 2.4.1 were triggered at the same location on the disk.

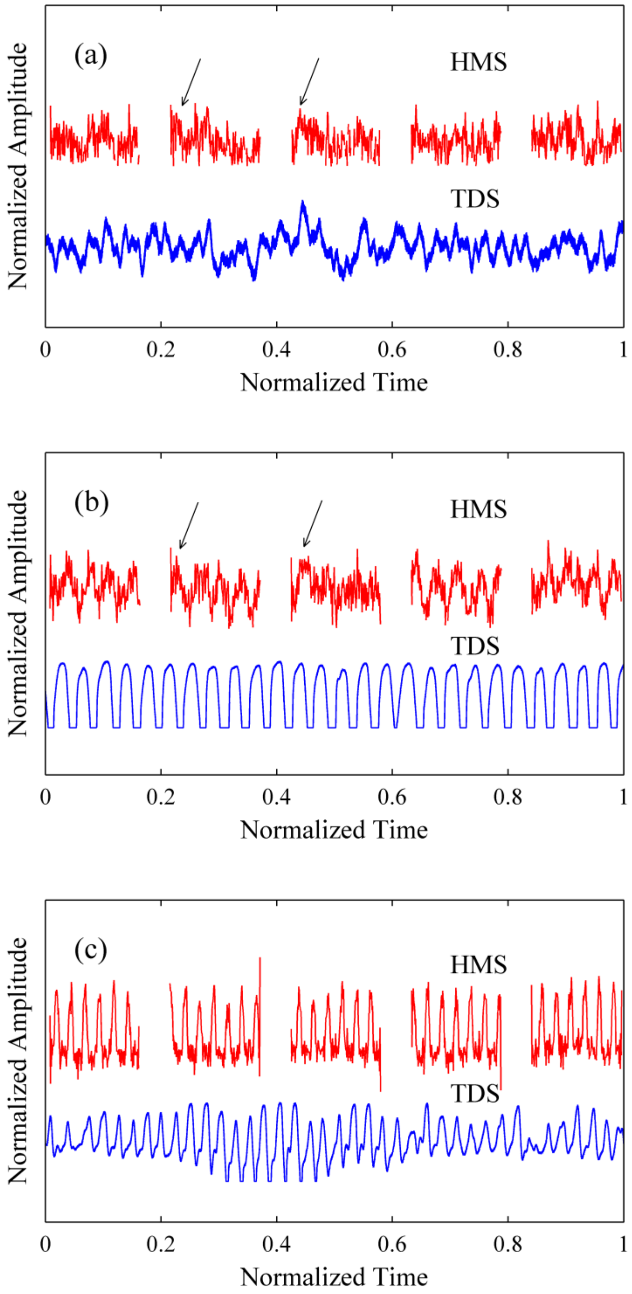

Fig. 2.4.1 HMS and TDS signal comparison at different stages: (a) passive flying stage, (b) transitional stage and (c) modulation stage.

Passive Flying Stage: In this stage, the HMS and TDS signals are both stable, repeatable and display irregular wave patterns (Fig. 2.4.1(a)). They are both related to the disk surface properties and correlate somewhat with each other. As the TFC power was increased, the standard deviation of the TDS signal was observed to increase exponentially, while the standard deviation the HMS signal showed a tendency to decrease (Fig. 2.4.2). The passive flying stage corresponds to TFC power from 0% TDP to 95% TDP.

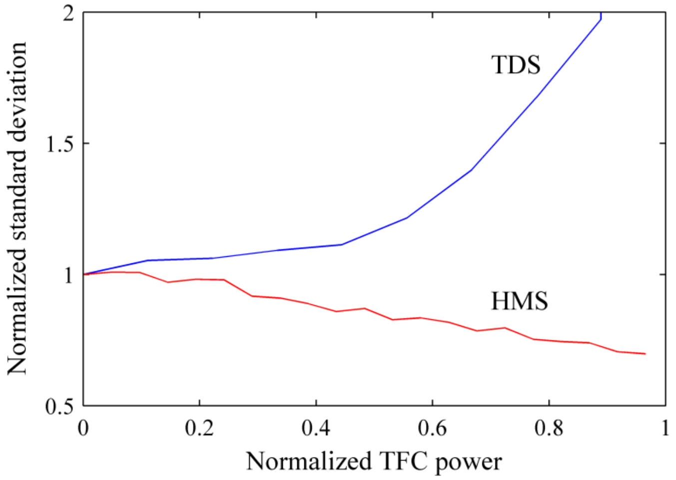

Fig.2.4.2 Standard deviation of HMS and TDS signal as TFC power increases during the passive flying stage

Transitional Stage: When the slider was flying at proximity, a transitional stage could be observed. In the transitional stage, the HMS signal showed a relatively low-frequency oscillating pattern added to the original HMS signal that shows disk surface information. The TDS signal at this stage also shows a ringing effect at the same frequency (Fig. 2.4.1(b)). Since the HMS signal is only related to the head–disk clearance, this wave pattern indicates that the head starts a vertical vibration in the transitional stage. In addition, the amplitude of vibration is still comparable with the surface microwaviness. In the TDS signal, however, the irregular wave pattern representing disk surface information is replaced by the modulation. This is probably because the temperature change caused by contact is much larger than the temperature change due to surface properties including microwaviness and moguls and the earlier pattern is suppressed. Combining the HMS signal and the TDS signal, it can be inferred that the air bearing surface (ABS) modulation starts in this stage, but the amplitude is much smaller than in the next stage. It may be concluded that the head is only in contact with the disk in some isolated regions instead of during the whole revolution, resulting in a comparably smaller amplitude of modulation. This stage usually appears when the TFC power is between 95% TDP and 110% TDP.

Over Push Modulation Stage: For the case of the TFC power above the transitional stage, apparent modulation can be observed from both the HMS and TDS signals. The HMS signal reveals periodic spikes, meaning that the head is bouncing on the disk surface. Between the HMS spikes, wave patterns of the disk can still be observed. In the TDS signal, however, the wave pattern is no longer observable (Fig. 2.4.1(c)). A possible explanation is that the contact-generated heat contributes much more to the temperature change than the microwaviness-generated air cooling effect. It was also observed that the frequencies of the TDS and HMS modulations increase with the increase of TFC power, indicating a change in the ABS modulation modes. In Fig. 2.4.1(c), the TDS signal showed a beating effect, meaning that at least two modulation frequencies are present. This modulation stage has also been reported in [49, 60].

In Fig. 2.4.3, the aforementioned stages can also be identified.

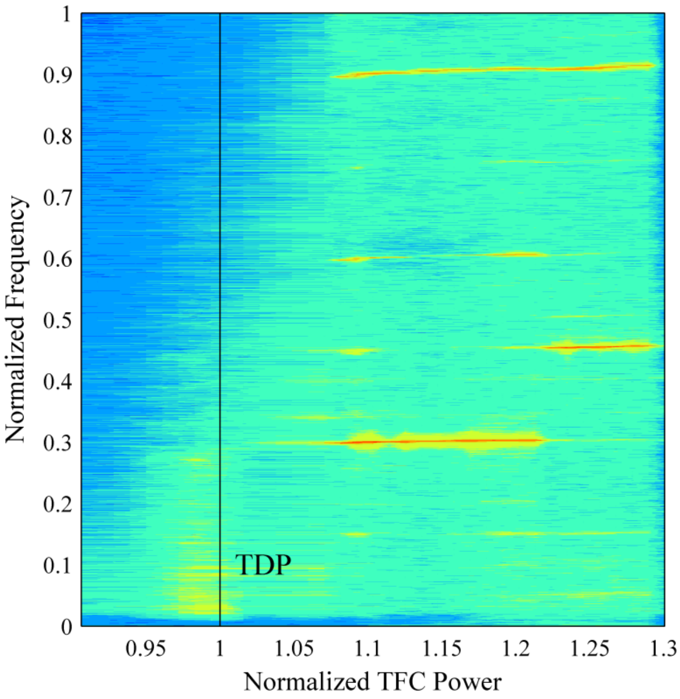

Fig. 2.4.3 Normalized TFC power-frequency spectrum contour of touchdown sensor signal

(a).When the TFC power is lower than 95% TDP, no obvious frequency exists in the frequency spectrum.

(b). A broadband amplitude rise in the frequency spectrum before touchdown corresponds to the transitional stage of TD.

(c). A modulation frequency and its second and third harmonics rise as the TFC power increases. More peaks in the frequency spectrum appear later, resulting in the beating effect in the time domain in Fig. 2.4.1(c).

2.4.2 Correlation between head-disk spacing and head temperature

When the head was flying with TFC power lower than the TDP, a repeatable pattern of TDS signal (index triggered) was observed. By comparing the TDS and HMS signals for the same time interval, we can observe similarities between the wave forms (Fig. 2.4.4). To quantitatively measure the similarity and the relative phase difference, we calculated the correlation coefficient between the HMS and TDS data points at each phase shift step (Fig. 2.4.5). In Fig. 2.4.5, it is seen that at a certain phase shift, the correlation coefficient between the HMS and TDS signals reaches a maximum of 0.748, and this number decays rapidly when the TDS signal is shifted either forward or backward. A clear correlation can also be seen in a scatter plot of the TDS and HMS data points at the optimum phase shift (Fig. 2.4.6).

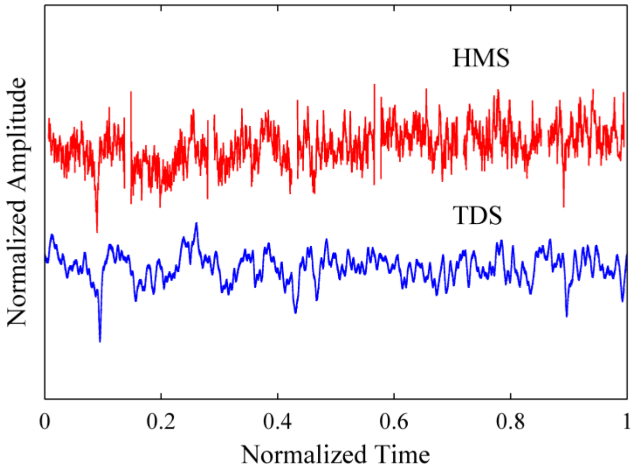

Fig. 2.4.4 HMS and TDS signals during passive flying

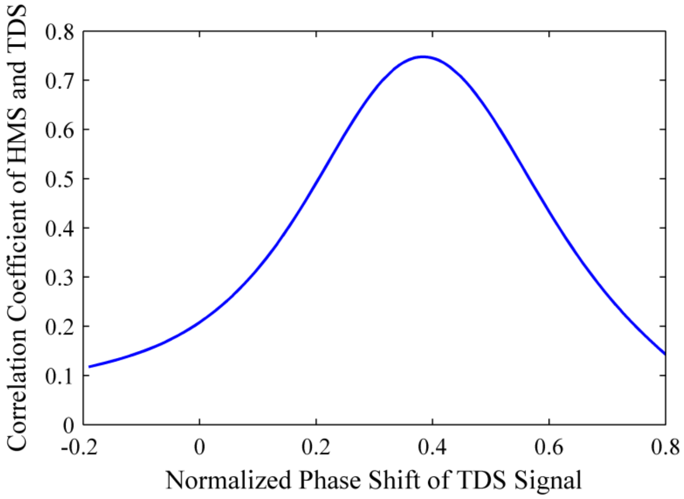

Fig. 2.4.5 Correlation coefficient between HMS and TDS signal with different phase shift

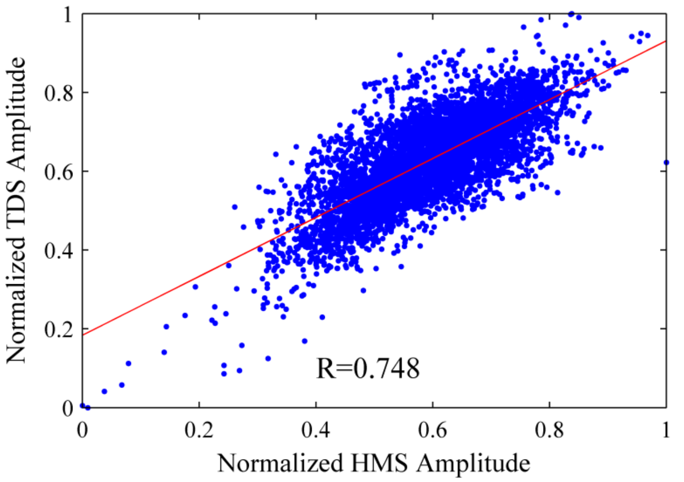

Fig. 2.4.6 HMS and TDS signal correlation at the best phase shift

In Fig. 2.4.6, both TDS and HMS signals are linearly shifted to the maximum correlation coefficient and normalized so that their minimum value during measurement is zero and maximum values are one. The positive correlation indicates that the temperature of the head rises as the spacing between the head and disk increases. This correlation between the TDS and HMS signals can be explained by the heat conduction dynamics in the HDI: when the flying height increases, the air cooling effect is less prominent on the slider, resulting in a slight temperature rise of the TDS, which is detected as a rise in the TDS signal. Similarly, a reduction in flying height - represented by a fall in the HMS - enhances the effect of air cooling and thus leads to a fall in the TDS signal.

This correlation demonstrates the possibility of using the TDS to identify and measure the HDI characteristics, including disk microwaviness and lube moguls. This result coincides with the result reported in [57].

2.4.3 Measurement of temperature response time using the correlation method

Since the TDS and HMS information could not be measured simultaneously at drive-level, another set of experiments were conducted on the component-level spin stand to further reveal the time delay in between the temperature response and flying status (Fig. 2.2.2). A challenge at the component-level is that the SNR is relatively lower, making it hard to correlate the TDS signal and LDV signal at the passive flying stage. Therefore, the over push modulation stage was chosen in this experiment because it had much more significant displacement and temperature response.

At over push stage (> 110% TDP), modulation is observed from both the spacing signal and temperature signal (Fig. 2.4.7). It is clear that these signals share the same modulation frequency, with a certain time shift.

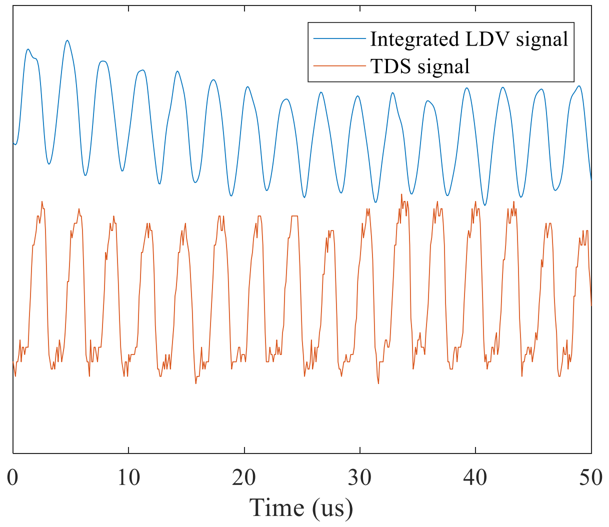

Fig. 2.4.7 Spacing (integrated LDV signal) and temperature (TDS) signal at 120% TDP over push stage

To determine whether the spacing signal and temperature signal are positively correlated or negatively correlated, and the time delay between these two signals, the co-correlation coefficient between these two signals with different time shifts were calculated (Fig. 2.4.8).

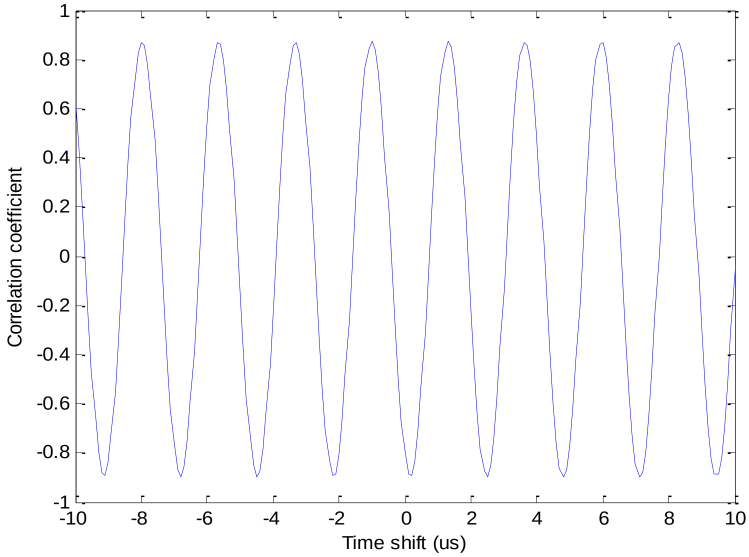

Fig. 2.4.8 Co-correlation coefficient between the spacing and temperature signals at different time shifts

Since both the integrated LDV signal and the TDS signals were sinusoidal with identical frequency, the co-correlation coefficient was also a sinusoidal curve. In Fig. 2.4.8, all of the maximum co-correlation coefficient points indicate a positive correlation at a specific time shift and the minimums indicate negative. Apparently, co-correlation between a single pair of signals is not enough to determine the real time shift, it is necessary to make use of the fact that the modulation frequency at over push will increase but the time lag between the signals should remain the same. In Fig. 2.4.9, the co-correlation coefficient as a function of time shift and TFC powers is plotted. From this contour, the change of the dominant modulation frequency at different TFC power is very clear. The fact that only one red stripe at around -1 μs is continuous from 100 mW to 135 mW in the contour clearly shows that the real correlation between spacing and temperature has a time delay of around 1 μs, and that these signals are positively correlated. A negative time shift means that the LDV signal happens earlier than the TDS signal in the time domain.

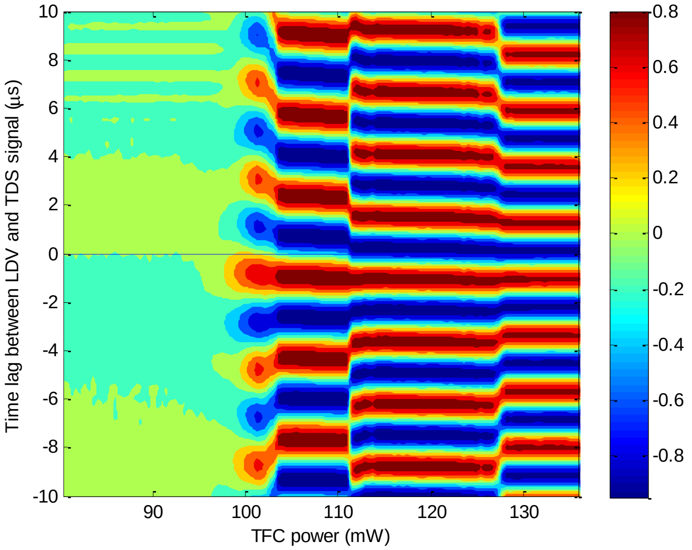

Fig. 2.4.9 Contour plot of Co-correlation coefficient as a function of time lag and TFC power

2.5 Summary and conclusion

In this chapter, the drive-level and component-level touchdown tests with high spatial resolution data acquisition were performed, and they were found to be an effective method for investigating different touchdown stages. Passive flying, transitional, and modulation stages were identified by TDS and HMS measurements from both the time domain and frequency domain. In the passive flying stage, both signals were repeatable and a correlation was observed between the two signals. This correlation proved that the TDS responds to the surface characteristics actively and sensitively. In the transitional stage and modulation stage, both the TDS and HMS lost their repeatability in the time domain due to modulation, but the frequency spectrum remained repeatable under the same TFC power. Along with the increase of TFC power during over push, the modulation frequency also increased, which was due to the change of ABS modulation mode. Meanwhile, identifying different touchdown stages with the TDS response can provide supporting details for failure analysis and tribology design in hard disk drives.

Establishing a correlation between the fly height and the temperature response can provide insights into the heat transfer model for the HDI. Both drive-level and component-level testing results showed that when TFC power remains constant, head temperature and flying height are positively correlated. When the flying height increases due to either disk surface microwaviness or contact induced modulation, the head temperature will increase as well, with a time delay of the order of microseconds. This further indicates a cooling effect as the head approaches the disk. This phenomenon will be studied in the following chapters.

Chapter 3 Measurement of nano-scale heat transfer with static touchdown experiment

3.1 Introduction

Many applications in nanotechnology require the understanding of heat transfer across nano-scale gaps between two bodies at different temperatures [20, 61-65]. In connection with the emerging data storage technology including HAMR and MAMR, CML has undertaken over the last decade both theoretical and experimental studies in nano-scale heat transfer.

As discussed in recently published papers [38-42, 66-68] classical methods[69] of calculating heat transfer are not valid at the nano-scale, because the underlying theories do not hold for nano-scale dimensions. The theories in Refs. [38] and [39], which are based on the wave character of both thermal radiation and phonon thermal conduction, have been shown to satisfy all known requirements for heat transfer across a closing gap as opposed to other presented theories[70-72], and it also is in agreement with such observed phenomena as Kapitsa resistance[73] of interfaces and the asymmetric phenomenon known as thermal rectification.

In Chapter 2, it has been shown that the head temperature is sensitive to the spacing between the head and disk and that a cooling effect is enhanced when the head disk spacing decreases. In order to further analyze the cooling effect and to test the validity of the published theories in Refs. 3 and 4, we sought an experiment for measuring heat flux across a gap between two bodies as the spacing between them closes in a controlled manner from 10 nm down to contact. While such a controlled experiment is notoriously difficult to perform, it is of great importance to measure the heat flux in such a nano-scale. Previous experimentalists have been striving to make measurements down to 20 nm [63, 74-76], and a recently published result which was able to control the spacing as close as 2 nm [77] was very well received. However, to fully verify the published theory, it is necessary to close the last 2 nm gap because according to the theory, the heat transfer coefficient will increase drastically when the gap size is within only a couple of nanometers.

In our effort to close the last 2 nm gap, the static touchdown experiments are designed with the read-write head (Fig. 3.1.1). In the read-write head, the TFC element is embedded in the end structure of Fig. 3.1.1(c). Placed near and a few microns above the write transducer, and between the read and write transducers nearer to the surface is the TDS. All of these transducers and sensors are connected to the wire harness shown in Figs. 3.1.1(a) and (b), and they are connected to various electronic instruments for measurements and control.

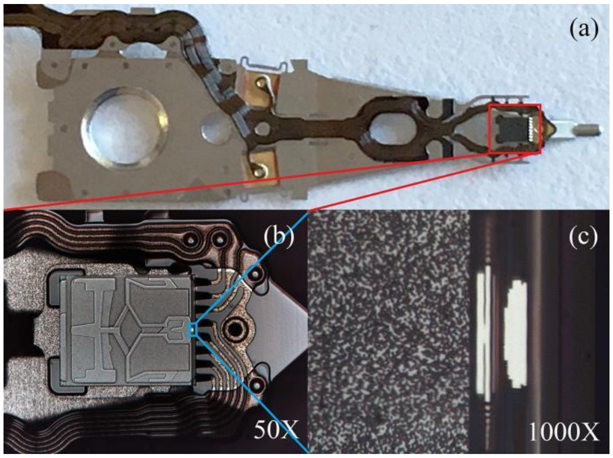

Fig. 3.1.1 Under side of the head and suspension showing (a) the slider-suspension structure; (b) the slider's air bearing design pattern, its suspension mounting, and its wire harness that connects to the various transducers. The dimensions of the slider block are about 820 x 700 x 230 µm. Its material is Al_2O_3-TiC. (c) is a zoom in of the right 20µm that carries the read-write transducers. The reader with shields is the left white portion; the writer is the right white portion. The transducers are embedded in Al_2O_3 and are made of such metals as Fe, Ni, Cu, and Cr.

This chapter presents a series of static touchdown experiments that was first performed on a silicon wafer to observe the temperature change of the interfaces during the process of closing the gap by supplying power to the TFC. Then the static touchdown experiments were performed under different conditions including vacuum and humidity environments and with different substrates with or without lubricant. These experimental results provided insights on the nano-scale heat transfer behavior in head media interfaces.

3.2 Methodology

3.2.1 Implementation of static touchdown experiment

A side view sketch (not to scale) of the experimental system and its photo are shown in Fig. 3.2.1 and Fig. 3.2.2. As depicted, the TFC is used to induce thermal expansion of a localized region for nano-scale spacing control, and the TDS is used to measure its temperature change due to the heat flux across the gap that occurs because of a temperature differential between the hotter TDS and the opposing plate. The slider block has a designed and fabricated crown of about 7 nm on its surface that opposes the plate. This crown together with the suspension connection and the TDS is critical for control of the gap.

During the experiments, the TFC heater shown in Fig. 3.2.1 raises the temperature in the structure that contains the TDS. This temperature increase causes a thermal protrusion that results in a spacing reduction between these elements and the surface on which the block is placed. The block can be rocked back and forth on its crown by use of a micrometer stage to move the wafer and thereby achieve a coarse adjustment of the initial spacing between the TDS and the test surface. According to our calculation from the geometry of the block, the maximum gap size change from rocking is 50 nm, which is sufficiently small when compared with the TFC protrusion size.

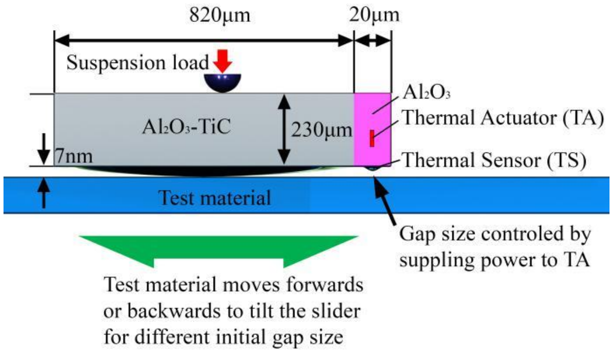

Fig. 3.2.1 Schematic of static touchdown experiment

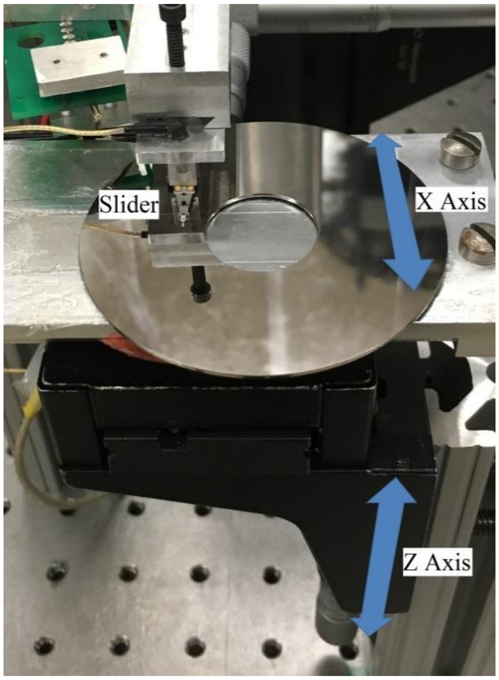

Fig. 3.2.2 Photo of experimental setup

Electronically, the configuration of the experiment is identical to that in Fig. 2.2.3.

In the static touchdown experiment, after setting the initial gap with the crown and micrometer stage, voltage is supplied to both TFC and TDS step by step. In each step, the TDS voltage is turned on 10 µs prior to TFC power to capture the transient temperature response of the TDS as the TFC turns on. Each step lasts 0.1 s to allow the head-media interface to establish static heat transfer. After each step, both the TFC and TDS are turned off to avoid accumulated system error. Fig 2.2.3 depicts a typical TFC and TDS voltage supply as the TFC power increases step by step from 10 mW to 100 mW.

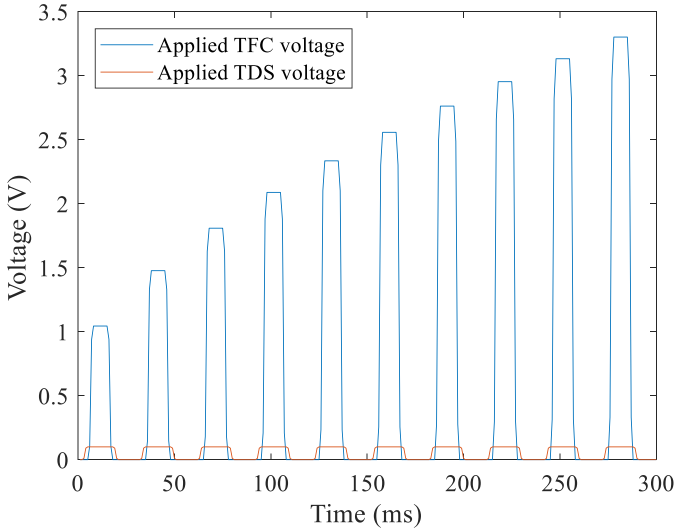

Fig. 3.2.3 TFC and TDS voltage supply in a typical static touchdown experiment

3.2.2 Environmental control

The existence of air molecules and an absorbed water layer affect the nano-scale heat transfer experiment extensively. It is necessary to control the temperature, pressure and humidity of the static touch down experiment to ensure a reliable experimental result.

By placing the whole setup in a vacuum chamber, pressure control can be achieved (Fig. 3.2.4). The chamber is connected in sequence to a turbo pump and a mechanical pump. When operating together, the chamber can reach high vacuum (HV, $<10^{-4}$ Torr). At such a pressure, the mean free path of air molecules is around 0.5 m. Thus we assume that no air molecule exists in the gap during the static touch down experiment.

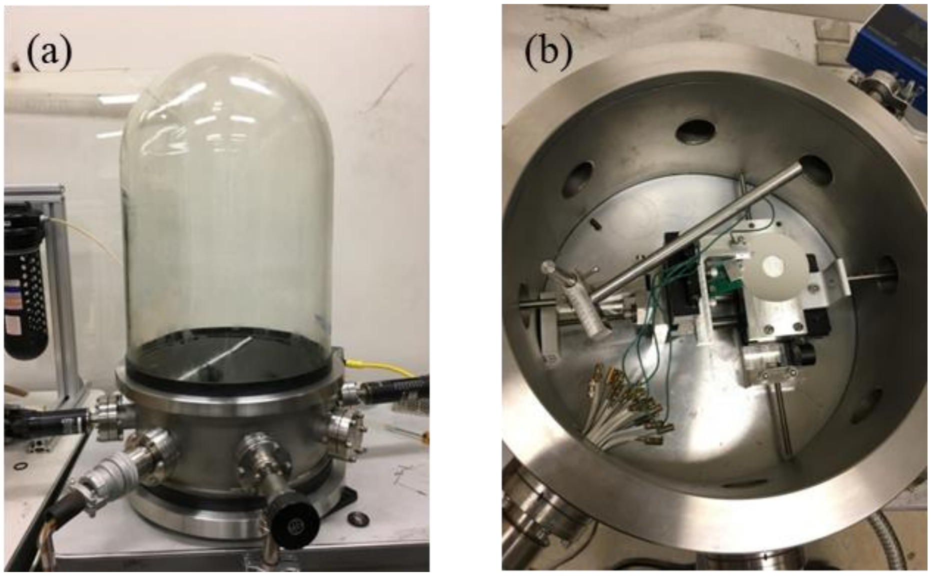

Fig. 3.2.4 Experiment setup of the environment chamber: (a) whole setup and (b) mechanical fixture for positioning control in the chamber

Temperature control of the test material is also important to further remove organic contamination and absorbed water molecules. A flat heater is located underneath the sample plate where the test material is located. A thermo-couple temperature sensor is located next to the test material to monitor the temperature of the test material in real time. Both the heater and the thermos-couple are connected to a temperature controller that controls the test material temperature using a proportional–integral–derivative (PID) algorithm.

Besides vacuum experiments, the chamber can also be used to control relative humidity (RH). To monitor RH, a RH sensor (HIH-5030-001) is installed inside the chamber. Higher RH is controlled with saturated salt solutions. With different saturated salt solutions, different relative RH can be achieved inside the chamber. For example, with a saturated sodium chloride solution inside the chamber, the equilibrium RH is 75% (Fig. 3.2.5). Lower RH is achieved by a series of flushing processes. First, the mechanical pump lowers the pressure of the chamber down to less than 1 Torr. Then, dry clean air filtered by desiccants is allowed to flow into the chamber. These two steps are repeated several times to reach a low RH (<5% RH).

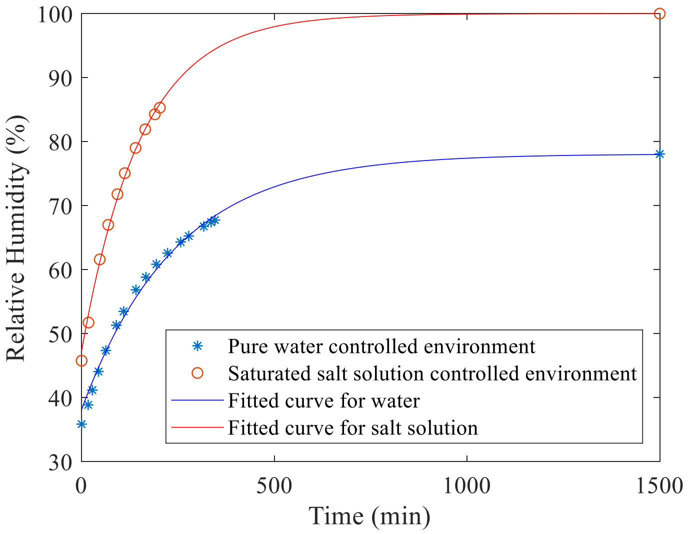

Fig. 3.2.5 Humidity control through saturated salt solution method

3.2.3 Lubricant removal

Magnetic disks with multidented lubricants were supplied by Western Digital Corporation. To study the effect of lubricant in the static touchdown experiment, some disks were de-lubed with 3M HFE-7100 solvent.

3.3 Results and discussion

3.3.1 Static touchdown experiment on silicon wafer

Fig. 3.3.1 shows several static touchdown experimental results. The top curve is the free space heating result for the case when the influence of the Si wafer is not present. It shows the rate at which heat is lost to the surroundings when the TDS is spaced at a distance sufficiently far from the wafer. This heat loss, which is mainly due to air convection from surfaces of the block, is treated as a baseline to be compared with heat loss due to phonon conduction when the gap size decreases.

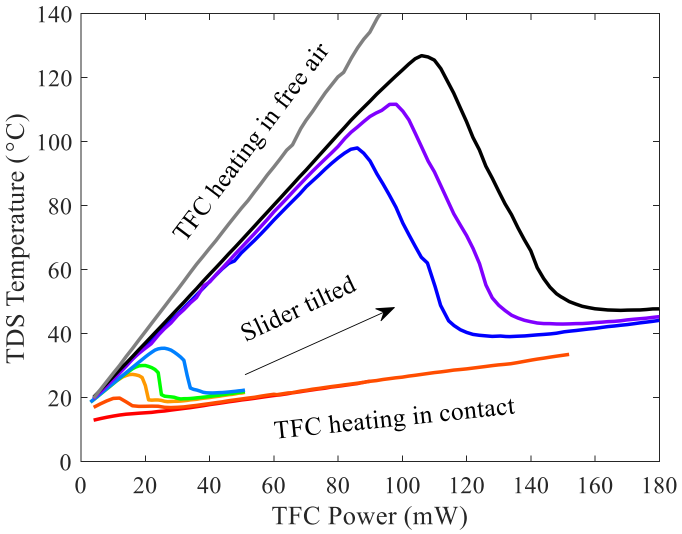

Fig. 3.3.1 TDS temperature change vs TFC power for the slider resting on the wafer as shown in Fig. 3.2.1. The slider tilt can be adjusted on its crown by a micrometer so that the initial spacing between the TDS and the wafer is only a few nm.

The next lower curves represent TDS heating experiments for different initial separations between the TDS and the Si wafer. The top most of these curves corresponds to a case where the initial separation was about 10–12 nm. According to an empirical TFC power – protrusion size relationship, 10 mW of TFC power corresponds to 1 nm of TFC protrusion. This ratio will be studied more carefully in chapter 4. The lower curves correspond to results for smaller initial separations. As can be seen, all of the curves initially show a linear increase of TDS temperature with an increase of TFC applied power. The TDS signal reaches a maximum (first heating region) and then reduces to a minimum (first cooling region) before again increasing linearly with TFC power (second heating region). The rate of TDS increase with TFC power in the second heating region is determined by the rate of increase of temperature when the TDS is in contact with the Si wafer. The amount of TFC power required for the TDS to reach a peak depends on the initial gap that is controlled by the initial positioning of the Si wafer by use of the micrometer stage.

The shapes of the curves in Fig. 3.3.1 show that the heat transfer coefficient increases drastically when the gap size reduces down to 1–2 nm. This accounts for the first part of the cooling region in the TDS vs TFC curves in Fig. 3.3.1 followed by the rapid decrease in TDS temperature until the contact condition is reached.

Still, there remains some question as to where contact occurs in the experimental results shown in Figs. 3.3.1. Indeed, there is a fundamental question about contact. We assume that contact does not mean that atoms of one surface touch atoms of the other surface, or that they are chemically connected to molecules or a crystalline structure. We understand that reaching contact is a continuous process, which starts when the surfaces become affected by intermolecular forces acting across a gap, and ends when a further increase of the pressure causes a disproportionally smaller effect on the observed properties of the structure. Because all of the curves in Fig. 3.3.1 drop to the same line that shows a linear increase with continued increase in TFC power, it is reasonable to conclude that this linear line represents the rate at which the TFC can increase the temperature of the TDS when the latter is in contact with the Si wafer.

The transient temperature responses in each step of static touchdown experiment are also worth investigating. In Fig. 3.3.2, the transient TDS signal at different stages of a static touchdown experiment are plotted.

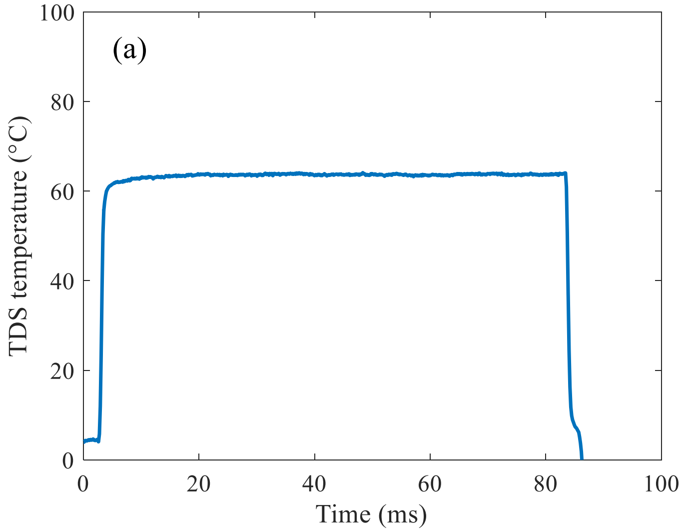

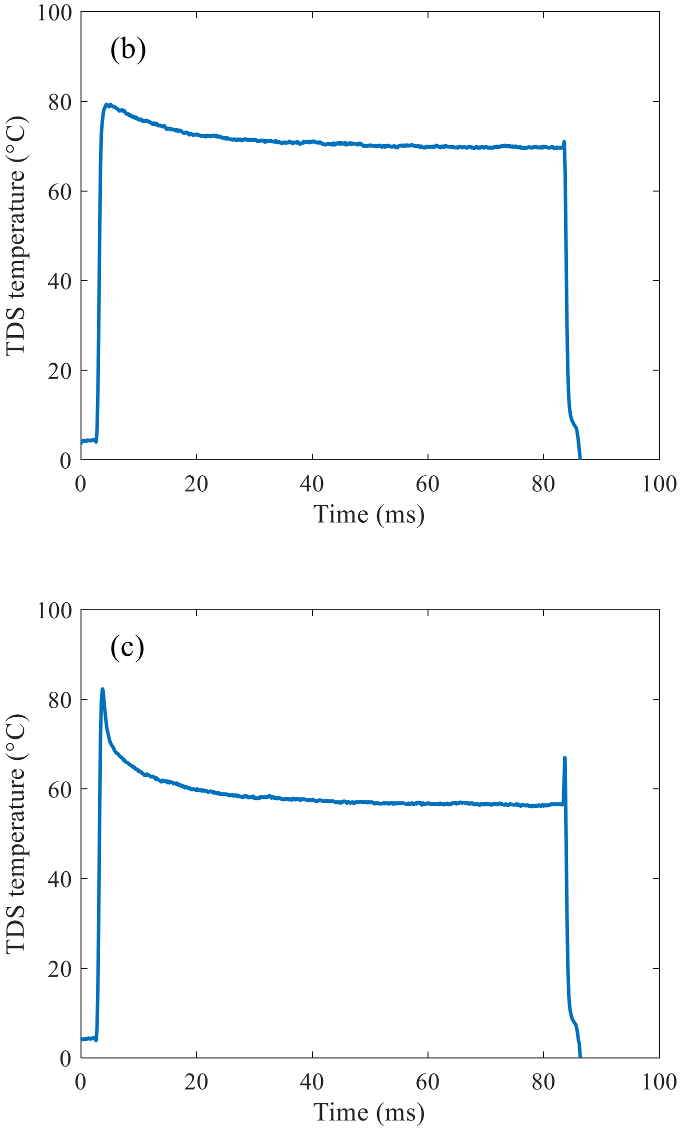
(b)
TDS temperature (°C)
0
20
40
60
80
100
Time (ms)
0
20
40
60
80
100
(c)
TDS temperature (°C)
0
20
40
60
80
100
Time (ms)
0
20
40
60
80
100

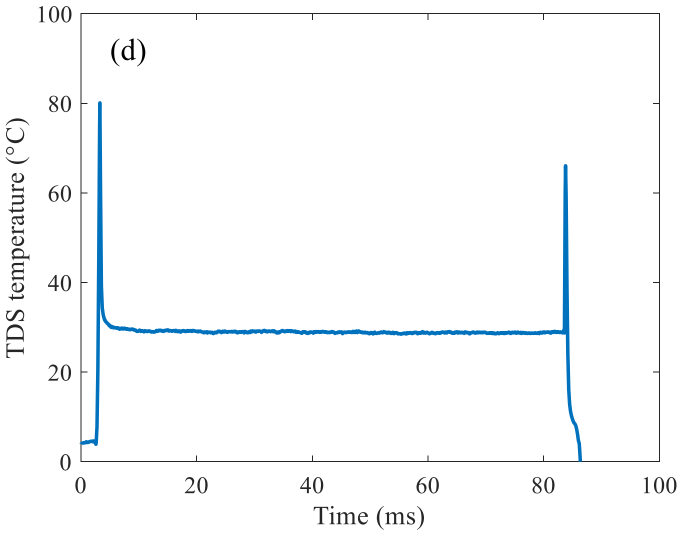

Fig. 3.3.2 Transient TDS response at (a) first heating region, (b) early cooling region, (c) late cooling region and (d) second heating region

In 3.3.2 (a), the TDS temperature increases to a higher step when the TFC power is turned on. This value remains constant until the TFC is turned off. In 3.3.2 (b), however, after rising to a peak value when TFC is turned on, the TDS temperature gradually decreases to a static value. When TFC is turned off, the TDS temperature shows a slight second spike up before dropping back. This change of curve shape can be explained by the process of TFC heating and TFC protrusion. When the TFC voltage is suddenly supplied to the head, the heat starts dissipating across the head and heats up the contact sensor; meanwhile, the TFC is protruding towards the disk and is losing heat to it. As the protrusion develops, more heat is lost to the disk, thereby reducing the protrusion process. As a result, the time interval between the maximum head temperature point and the constant value represents the time required to establish a steady state. In 3.3.2 (c) and (d), the same spikes still exists, but at higher TFC power, the time required to establish steady state reduces significantly.

Another series of experiments, called here load-unload experiments, was conducted to shed more light on this contact question. In these experiments, the TFC power was linearly increased to a certain value and then decreased at the same rate. The results are displayed in Fig. 3.3.3, where the initial starting position was only about 3 nm from the Si wafer. As shown in Fig. 3.3.3, the TDS temperature increased and decreased along the same line as the TDS protrusion was increased up to about 3.2 nm. If, however, the TFC protrusion was increased slightly more to about 3.5 nm, there occurred a hysteresis loop in the load-unload curve. This loop was more pronounced if the maximum TFC protrusion was about 3.7 nm, and substantially more pronounced if the TFC protrusion reached 4 nm. Finally, when the TFC protrusion reached 4.2 nm, the unload curve first traversed a short segment of the linear contact curve of Fig. 3.3.3 in its unload path. The hysteresis loop is caused by the van der Waals force. When the protrusion approaches the wafer, the protrusion will first be within the range of van der Waals force before full contact. During the unload process, however, the van der Waals force will keep pulling the slider, therefore causing the hysteresis loop. It is remarkable that these experiments are repeatable, and show distinctive differences when one realizes that the protrusion differences are only about 0.2 nm between them. We conclude from this series of experiments that the lower linear TDS temperature versus TFC protrusion envelope curve defines the contact conditions for the sequence of experimental results shown in Fig. 3.3.3.

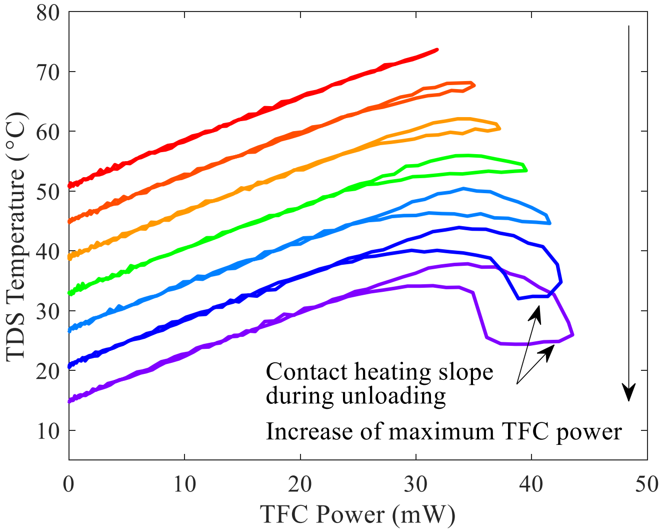

Fig. 3.3.3 Load-unload experiments showing the onset of contact; the TDS temperature scale is for the bottom curve. The other curves are uniformly shifted up for clarity.

3.3.2 Comparison to touchdown experiment on a flying disk

For comparison purposes, a touchdown experiment was first conducted on a rotating disk, followed by the static touchdown experiment, with the same head and disk. The changes of contact sensor resistance with TFC power in the two experiments are plotted in Fig. 3.3.4. It is clear that in both cases, the TDS resistance goes through the first heating region, the first cooling region and the second heating region.

According to [57], the first and second heating region of the curve in Fig. 3.3.4(a) obtained from a flying experiment are caused by TFC heating and sliding contact frictional heating, and the cooling region is solely due to air cooling. However, this explanation fails for Fig. 3.3.4(b), because on a non-rotating disk, there is no air flow and no extra pressure in the HDI. Under this static condition, a conventional air conduction model for the gap cannot be applied because even in normal room air, there are not enough air molecules within the 2 nm gap to support the convection model.

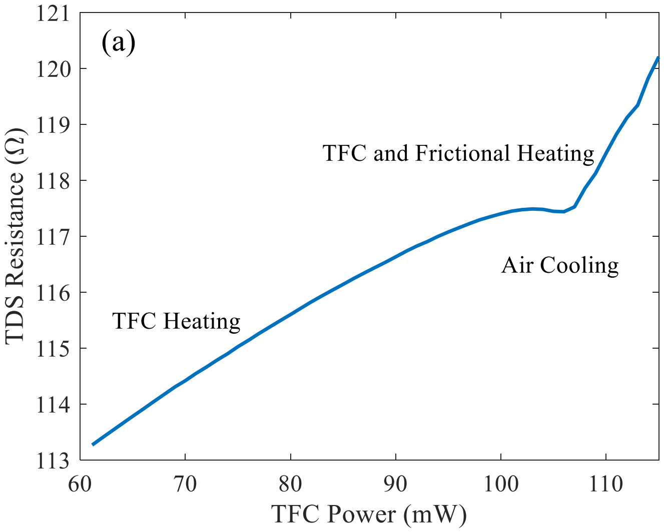

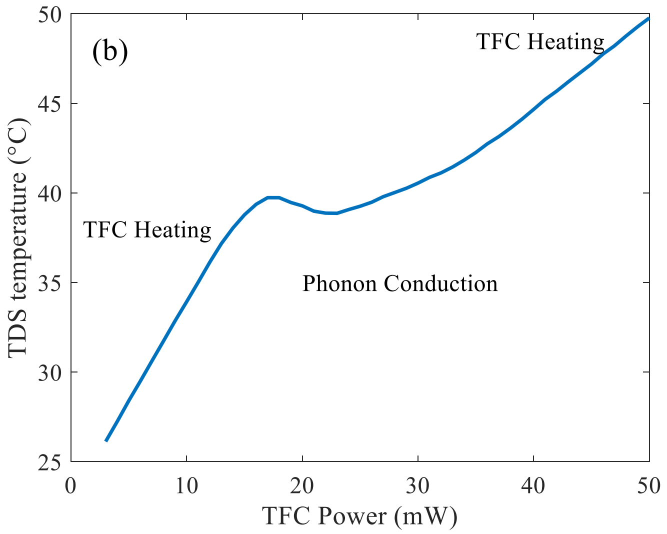

Fig. 3.3.4 TDS resistance change with increasing TFC on (a) a rotating disk and its air-cooling-based explanation and (b) a static disk with tis phonon-cooling-based explanation

From the wave-based phonon conduction theory [38, 42], the heat transfer coefficient across a closing gap increases drastically when the gap size is within only a couple of nanometers. As the clearance between the head and disk reduces to around 1 or 2 nm, the heat flux between the head and the disk increases rapidly, causing this drop in head temperature. After the head is completely in contact with the disk, the head temperature again increases due to further TFC heating.

It is also noticeable in Fig. 3.3.4(b) that the starting slope of the curve is higher than the ending slope of the curve. This is because at lower TFC power, the head is not in contact with the disk and heat loss to it is comparatively small. When the TFC power is high enough to drive the head into contact with the disk, heat loss to the disk is much higher and the same amount of TFC power increment causes less temperature rise in the head. The cooling region between these two heating regions corresponds to the drastic increase of heat flux when the head disk clearance falls to 1-2 nm.

3.3.3 Effect of humidity

In studying nano-scale effects, one of the most important factors that may affect the results is the existence of air molecules and humidity. Therefore, static touchdown experiments were conducted in both humid environments and dry environments. Single crystal Si wafers are used as the test material in this set of experiments.

Static touchdown experiments are performed at different RH levels including 16%, 31%, 75% and 100% (Fig. 3.3.5).

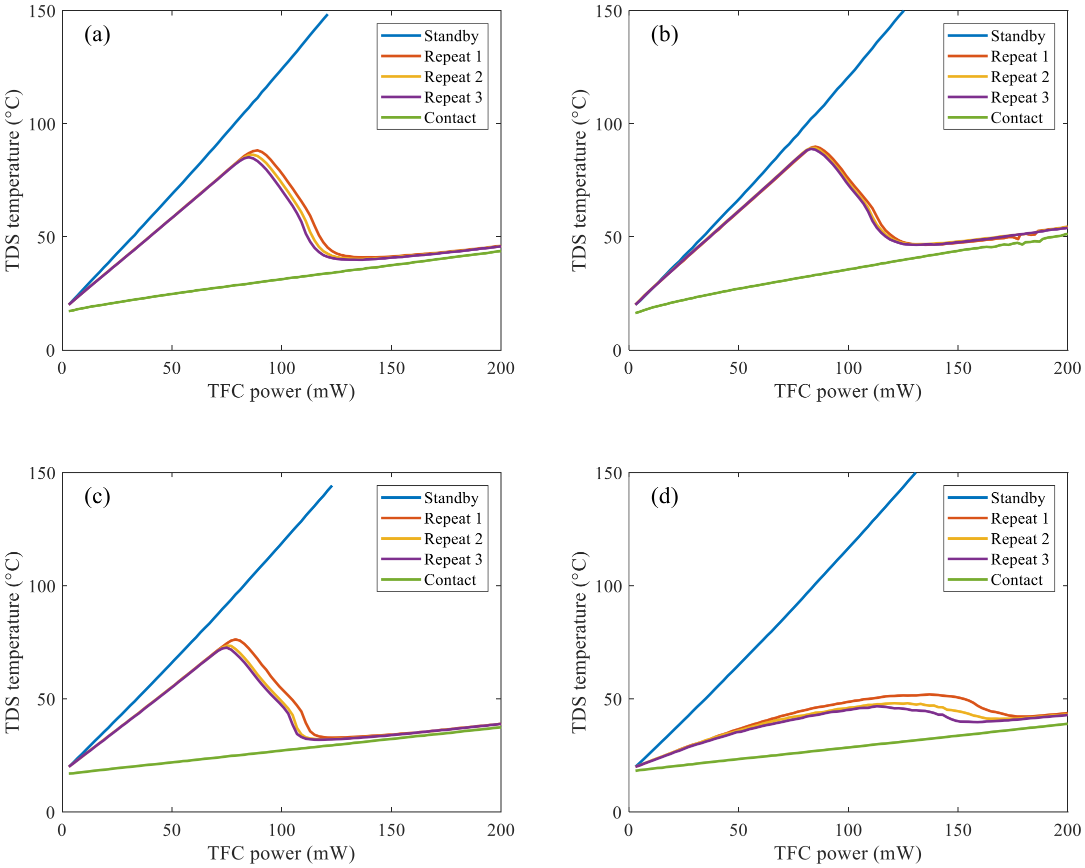

Fig. 3.3.5 Static touchdown experiment results at 760 Torr in (a) 16% RH, (b) 31% RH, (c) 75% RH and (d) 100% RH at 20 ℃.

In all of the four subplots of Fig. 3.3.5, the top blue curves are the free heating curve, obtained when the head is located sufficiently far away from the Si wafer. The bottom green curves are obtained when the TDS is directly in contact with the wafer. While the transitional curves indicating the closing gap process in Fig. 3.3.5 (a), (b) and (c) have identical slopes at the first and second heating regions, the cooling regions are slightly different: as the RH increase from 16% to 75%, the curve of the cooling region deforms from a smooth fall to a two-stage fall, depicting a hump in the middle of the cooling curve. Fig 3.3.5(d) is further discussed seperatly at the end of this section.

According to the load-unload experiment in section 3.3.1, the head contacts the wafer at the local minimum temperature point. To better compare the shape of the curves in the first cooling region, these three curves are aligned with each other at the contact point and replotted in Fig. 3.3.6, which shows that at 75% RH, the heat transfer from the head to the disk is first impeded and then accelerated, depicting two cooling regions with different dropping slopes: when compared with the case of 16% RH, the first cooling region of 75% RH has a lower temperature decreasing rate as the TFC power increases, but after the turning point at around 124 mW TFC power, the temperature decreasing rate becomes larger and the TDS temperature drops rapidly to the local minimum temperature.

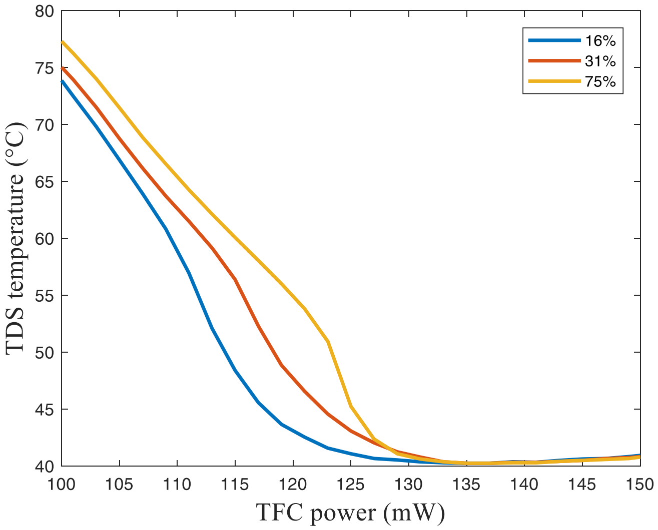

Fig. 3.3.6 Realigned static touchdown experiment results of 16% RH, 31% RH and 75% RH to compare the cooling region

The transient response of the process is also investigated. For the 75% RH case, the transient response of the TDS temperature at the first heating region, first cooling region (cooling region where the TFC power is less than 124 mW), second cooling region (cooling region where the TFC power is larger than 124 mW) and second heating region are separately plotted in Figs. 3.3.7 (a)~(d).

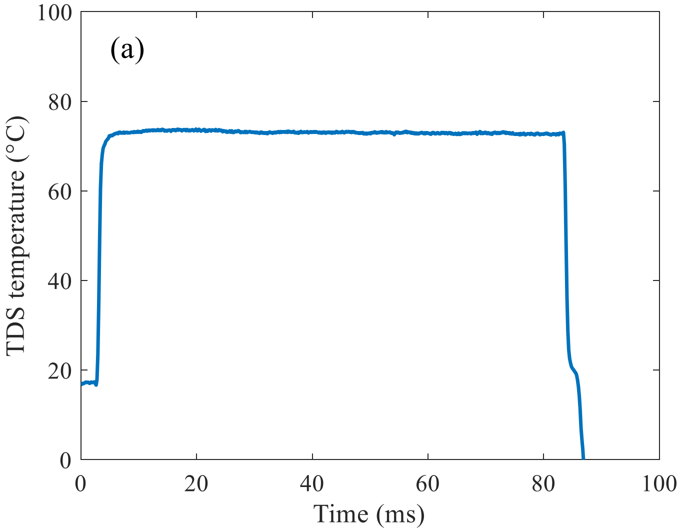
(a)
TDS temperature (°C)
Time (ms)
0
20
40
60
80
100
0
20
40
60
80
100

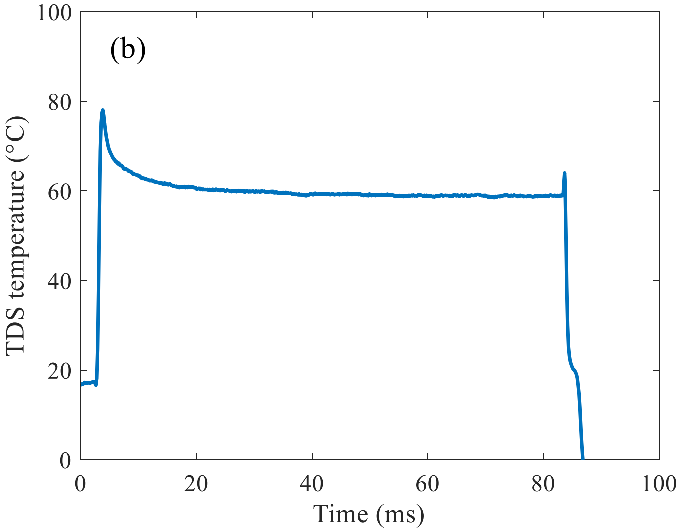
(b)
TDS temperature (°C)
Time (ms)
0
20
40
60
80
100
0
20
40
60
80
100

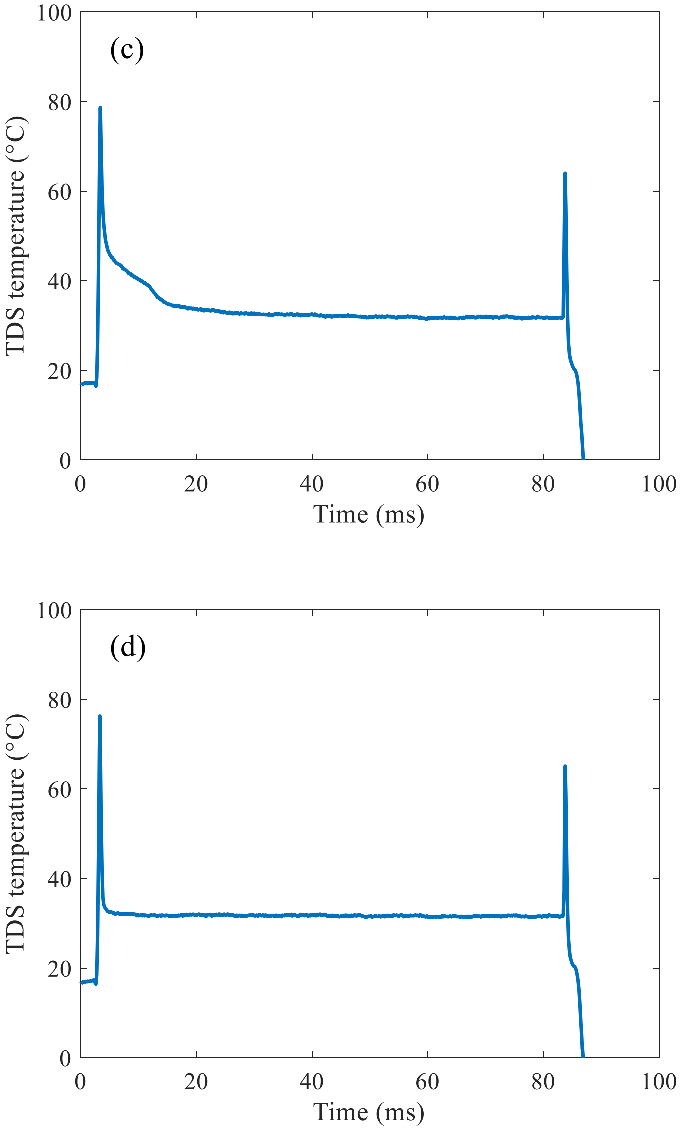

Fig. 3.3.7 Transient response of the TDS temperature at (a)first heating region, (b) first cooling region, (c) second cooling region and (d) second heating region

In Fig. 3.3.7 (c) a step temperature drop after the exponential drop is clearly visible. A possible explanation of this result is that before the turning point at 124 mW TFC power, the TDS is not in contact with the water layer, and the water layer acts as an impedance of heat transfer between the head and disk. After the TFC protrusion is high enough to drive the TDS into the water layer, the water layer accelerates the heat loss from the head.

In the case with 100% RH (Fig. 3.3.5 (d)), although the curves still depicts two heating regions and one cooling region, the slope of the first heating region is apparently lower than the other three subplots. It is believed that at this humidity, the water layer is thick enough to fill the initial gap between the head and disk, therefore the heat loss curve of the TDS is completely different from the other cases. Previous studies have shown that absorbed water layers can form on silicon wafers and disks and that the thickness of the water layers change with RH [78-80]. It is also mentioned in the paper that at 100% RH, the water layer, at the thickness of 3 nm, behaves more like liquid whereas at lower RH, the absorbed water layer behaves 'Ice like' [78].

3.3.4 Effect of air and vacuum

A static touchdown experiment result in vacuum and its comparison with a standard pressure experiment result are plotted in Fig. 3.3.8.

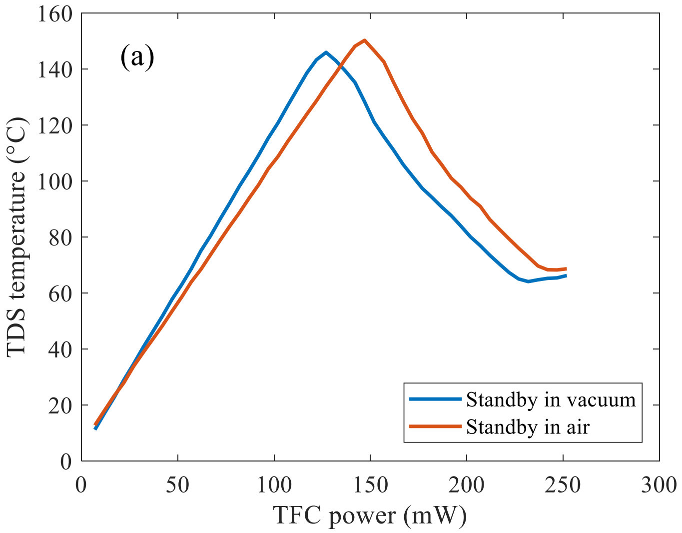

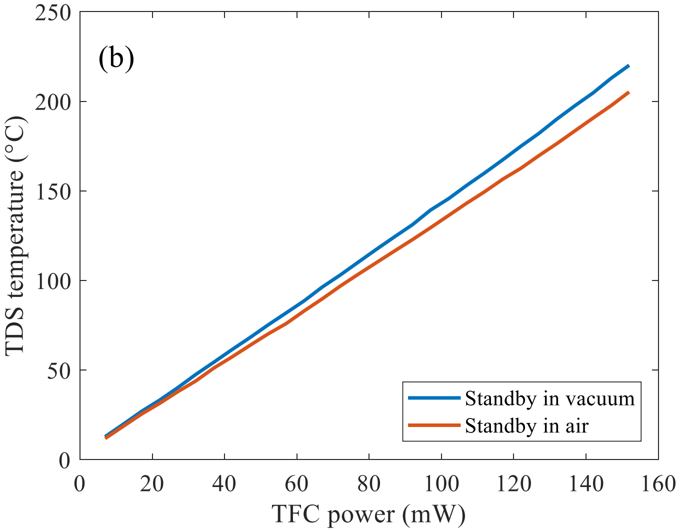

Fig. 3.3.8 Comparison of static touchdown experiment in high vacuum and standard pressure (a) contact process and (b) standby comparison

Fig. 3.3.8 (a) was acquired through the following process. First, a static touchdown experiment was performed in high vacuum environment with a specific initial gap. Then, the chamber is instantly ventilated with dried clean air. The result for the standard pressure was captured within less than one minute from the high vacuum experiment. From Fig. 3.3.8, two significant differences can be observed between the curves.

1).In high vacuum, the slope of the first heating region is larger than in the standard pressure case. This difference corresponds to the heat loss through free air convection.

2).In high vacuum, the cooling region appears earlier than the standard pressure case, with a lower maximum temperature. Since free air convection is not present in high vacuum, the same amount of TFC power could generate a slightly larger protrusion in high vacuum. Therefore, both the first cooling region and the second heating region appear earlier in high vacuum case.

3.3.5 Effect of lubricant layer

The static touchdown experiments were performed on both lubed and de-lubed magnetic disks. While the head temperature goes through a similar heating-cooling-heating cycle in both cases, several differences can be observed in the experimental results to demonstrate the effects of the lubricant.

After setting a relatively small initial head-disk clearance on a disk with lubricant, a series of touchdown experiments were performed within a short period of time (< 10 mins) and the results are plotted in Fig. 3.3.9 (a). Similarly, a set of results on the de-lubed disks are plotted in Fig. 3.3.9 (b).

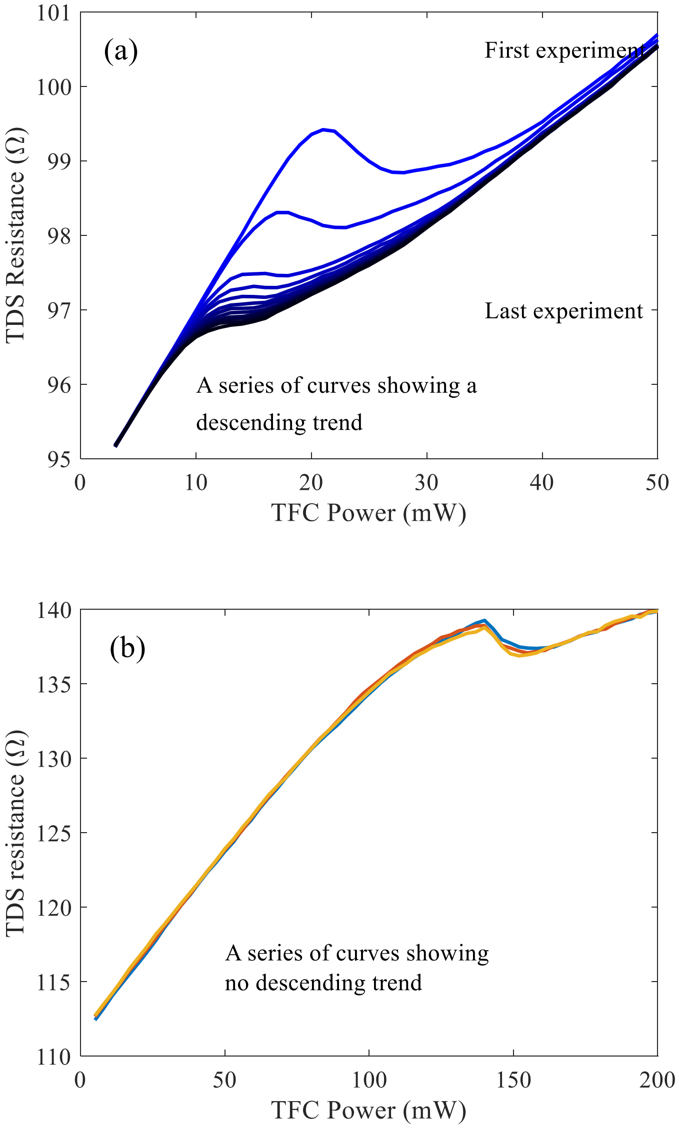

Fig. 3.3.9 Repeated static touch-down experiments on: (a) lubed disk, and (b) de-lubed disk

In Fig. 3.3.9(a), a descending trend of the touchdown curves can be observed. In the first static touch down experiment, the first heating region, cooling region and the second region are very distinct. In the last experiment, however, there is almost no observable cooling region. On the de-lubed disk (Fig. 3.3.9(b)), such a descending trend could not be observed over repetitions of the experiments. Therefore, a possible explanation is that through repeating the experiments, the head picks up more and more lubricant during each contact, changing the interface throughout the series of experiments.

Significant difference can also be observed from the transient response of the TDS at the cooling region. On a de-lubed disk, the head temperature first rises and then gradually drops to a lower constant value (Fig. 3.3.10 (a)). The time duration of the drop portion decreases with increasing TFC power. On a lubed disk, the dropping period is replaced by a step (Fig. 3.3.10 (b)). Similar to the case on de-lubed disks, the duration of the step narrows with increasing TFC power until it becomes a sharp drop.

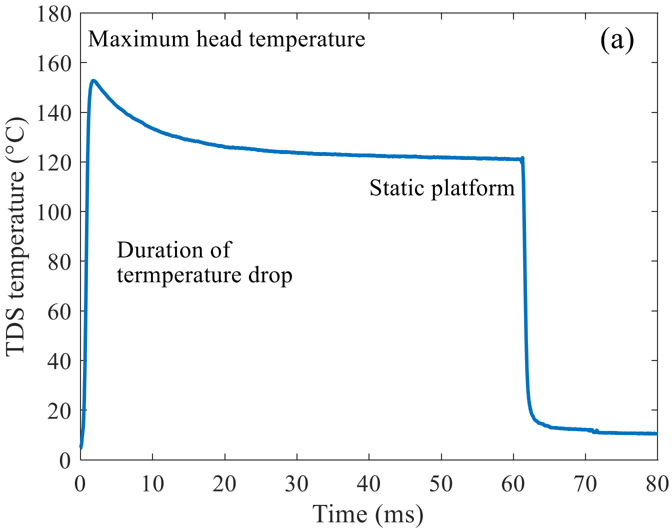

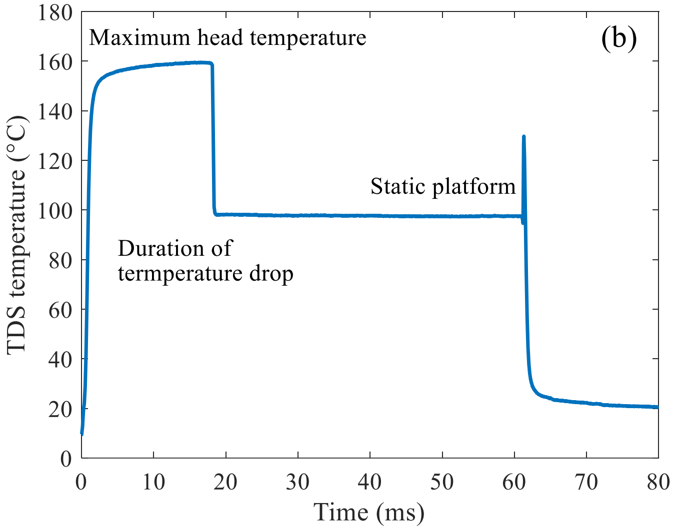

Fig. 3.3.10 Transient response of TDS change during static touchdown experiment on (a) a de-lubed disk and (b) a lubed disk

A possible explanation for the sharp drop in the lubed disk case is that the heated head is first supported by the lubricant for a short period until it 'melts through' the lubricant or possibly in combination with a water molecule layer in the vicinity and gets into direct contact with the disk. How the lubricant layer deforms and recovers is not exactly clear at this point.

3.3.6 Effect of disk substrate

On different substrates, the slope of the second heating region in the static touchdown experiment is significantly different. With a better heat conductor (higher heat transfer coefficient), the slope of the second heating region will be lower, because at the second heating region, the TFC power not only needs to locally heat up the head, it also needs to heat up a small portion of the disk that is in contact with the disk. If the disk is a good heat conductor, the same amount of TFC power will correspond to a low TDS temperature at contact. Static touchdown experimental results on a Si wafer, PMR disk with aluminum substrate and PMR disk with glass substrate are plotted in Fig. 3.3.11.

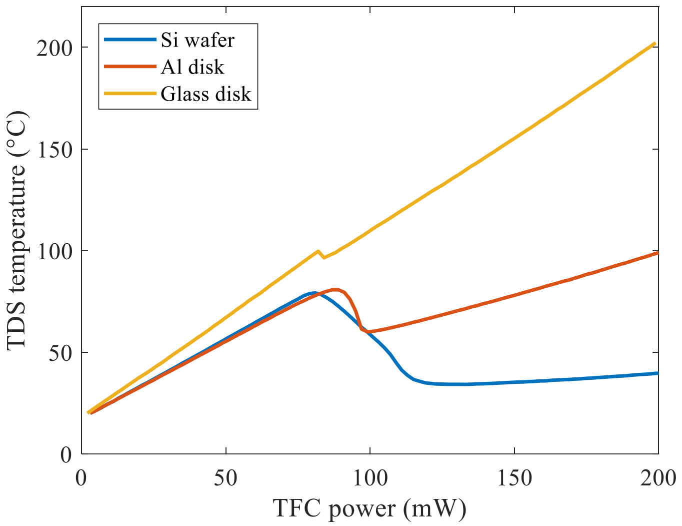

Fig. 3.3.11 Static touchdown experimental results on a Si wafer, PMR disk with aluminum substrate and PMR disk with glass substrate

As can be observed from Fig. 3.3.11, the Si wafer is a better conductor than both the PRM disk with aluminum substrate and glass substrate. While aluminum itself has a higher heat transfer coefficient than silicon, the existence of the DLC layer and magnetic layer impedes heat transfer through the disk. The PMR disk with a glass substrate shows a very small drop at the head-disk contact, indicating that the glass substrate disk has poor performance on heat conduction. It is also noticeable that the slope of the first heating region on the glass disk is slightly higher than on the other two. Since heat loss of the head in the first heating region is not yet dominated by phonon conduction, this result indicates that radiation heat transfer between the head and disk already exists when the gap size between the head and disk is around 10 nm, and that radiation heat transfer is also sensitive to the materials. These observations lay the foundation for utilizing the static touchdown experiment as a standard method to measure the material properties, including heat transfer coefficient and emissivity. Since the TFC protrusion size is on the scale of 10 μm and the TDS is even smaller, this method could be improved to measure the heat transfer coefficient of small features including grains, thin films or other micro-scale structures that are usually challenging to measure with conventional methods.

The influence of the disk substrate can also be compared with the flying experiments. In Fig. 3.3.11, TFC power is increased from 60 mW to 150 mW on a rotating disk on the same track at 7200 RPM. The cooling effect on a PMR disk with a glass substrate is much less significant than that with an aluminum substrate. The second heating region is also different: on a glass substrate, this region is relatively smooth, with a larger slope than the first heating region, whereas on the aluminum substrate, this heating region is wiggly, with an average slope smaller than the first heating region.

From chapter 2, it was shown that at the over push stage, modulation appears at the head disk interface. With such complicated head-disk spacing change, the temperature response at such stage is affected by not only frictional heating, but also heat flux variation with respect to the head-disk spacing change during modulation. According to Fig. 3.3.12, heat flux increases significantly on a static PMR disk with aluminum substrate, but it is not significant on a static PMR disk with glass substrate. Meaning that on an aluminum substrate disk, the head temperature is more sensitive to the head-disk spacing than on a glass substrate disk. This could explain why the second heating region on a glass substrate disk is smoother than the aluminum substrate disk, and with a higher slope.

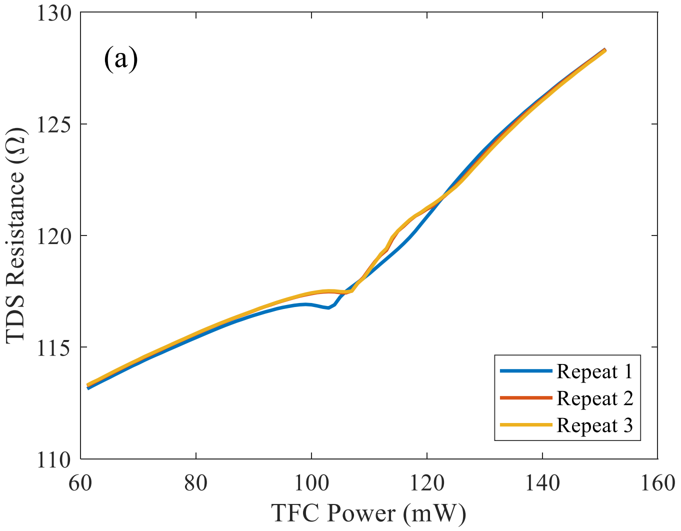

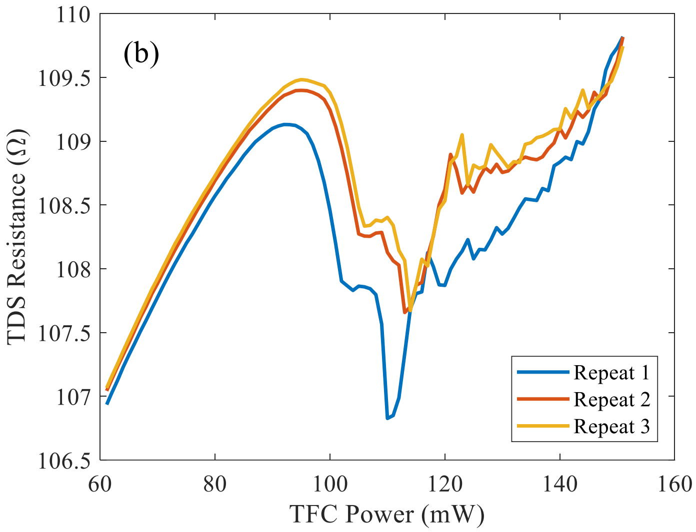

Fig. 3.3.12 Comparison of an overpush process on (a) PMR disk with glass substrate and (b) PMR disk with aluminum substrate

3.4 Summary and conclusion

In this chapter, the methodology of the static touchdown experiment is introduced and the heat transfer behavior is observed across a closing nano-scale gap between a head and disk in which the spacing is controlled in the nano-scale range down to less than one nanometer and into contact. The observations of enhanced heat transfer at the closing gap are in general agreement with the theoretical predictions of the wave based theory for radiation and phonon conduction. And the measured results compare well with the theoretical development that can explain the experiments without some ad hoc adjustments for each individual case.

Different factors, including humidity, air pressure, lubricant layer and disk substrate and their influence on the head-disk nano-scale heat transfer are studied separately. With higher humidity, the existence of an absorbed water layer impedes the heat transfer between the head and disk when the gap size is less than a couple of nanometers.

Comparison between the experimental results in high vacuum and standard pressure showed that while the influence of air convection on the head-disk heat transfer is clear enough to be observed under this controlled experiment, it does not affect the shape of the temperature-TFC protrusion curve.

Experiments on lubed and de-lubed disks showed that the lubricant affects the static touchdown experiments in two ways with different head temperatures. When the head temperature is relatively low, the head picks up lubricant in repeated heating and cooling cycles; when the head temperature is high, the head appears to “melt through” the lubricant.

Experimental results with different disk materials are also compared. While these static touchdown curves all exhibits one cooling region between two heating regions, the slopes of the two heating regions are distinctively different. The difference in slope of the first heating region reflects the radiation heat flux difference and the slope of the second heating region reflects heat transfer coefficient. This experimental observation lays the foundation to utilize the static touch down experiment as a standard material property characterization method.

Chapter 4 Simulation of nano-scale heat transfer behavior in static touchdown experiment with wave-based heat transfer theory

4.1 Introduction

In Chapter 3, static touchdown experiments showed that the wave based phonon conduction heat transfer coefficient in a nano-scale gap like the HDI is much larger than traditionally expected, and it can cause significant heat transfer across the HDI [81-84]. Qualitatively, these experimental observations match the theoretical prediction of the wave based phonon conduction. However, the wave based phonon conduction theory and most other near-field radiation theories are based upon very simple geometries like infinite half spaces. These theories can not be readily applied to the complicated geometries of a real head disk interface. In the static touchdown experiment, the shape of the TFC protrusion greatly affects the overall heat flux from the head to the disk. So the two half-spaces simplification is not accurate enough. Determining the head-disk clearance in a static touch down experiment is also crucial for interpreting the experimental results. Previously we only have the estimation of 0.1 nm/mW TFC protrusion rate based on flying heads. It is known that when flying, the TFC protrusion will cause a ‘push back’ to the whole slider [85]. Meanwhile, the results in Chapter 2 and 3 showed that at contact proximity, heat loss from the head is more severe, indicating that the TFC protrusion is not a perfect linear function of TFC power. Considering all these factors, it is necessary to develop a simulation method that incorporates both the heat transfer theory and the complicated head disk geometry.

Previously, many numerical methods to analyze the HDI dynamics and heat transfer behavior have been developed to simulate the head deformation [86-88], lubricant deformation [89-91], dynamical response [92, 93], temperature change [85] and shock response [94-96] of the HDI. However, these methods do not take into account the increased heat flux due to phonon conduction and are not applicable to static touchdown experiments.

Therefore, to improve our understanding of the heat transfer behavior in the HDI, it is necessary to build a numerical model of the HDI that takes into account both the wave based phonon conduction theory and the complexity of head disk interface. In this chapter, the method for incorporating the wave based phonon conduction theory into the FEM is first introduced, followed by the simulation strategy. Next, the simulation parameters are calibrated by a free TFC protrusion measurement. Finally, results generated by this simulation are presented and compared to the experimental results. This simulation method also has the potential to be applied to analyze the transient response of the TDS temperature, the static TDS response of flying heads and head temperature distribution in HAMR conditions.

4.2 Integrating wave-based heat transfer theory into FEM

To calculate the heat flux between two infinite half spaces with different temperatures, both radiation and phonon conduction contributions are considered. The total heat flux is calculated according to [82, 83] in Section 1.4.

While implementing this full equation into FEM is possible, the calculation is too time consuming. Therefore, the heat flux calculation is equivalently converted to a convectional heat transfer process and the equivalent heat transfer coefficient between the two half spaces is approximated by a function of gap size (h), temperature of the cold surface (T_0) and the temperature difference between the two surfaces (ΔT) (Fig. 4.2.1). In Fig. 4.2.1, the equivalent heat transfer coefficient is linear in h and ΔT on a log-log plot: with smaller gap size and temperature difference, the heat transfer coefficient increases drastically. The equivalent heat transfer coefficient is a linear function of T_0.

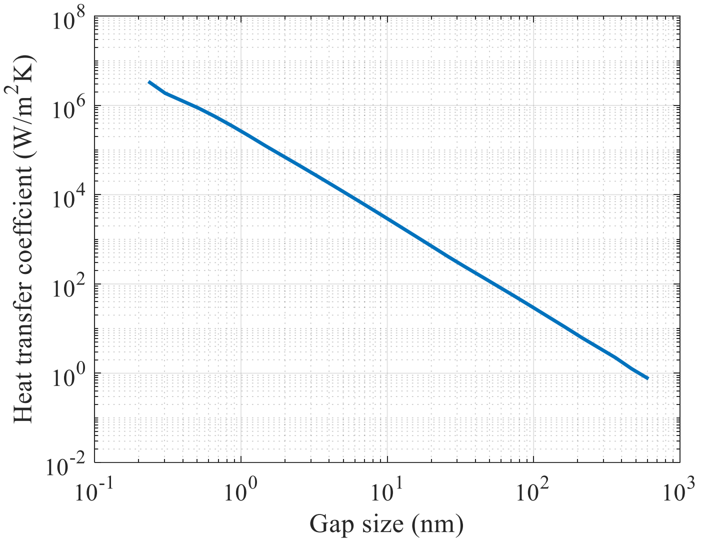
Heat transfer coeffcient (W/m^{2}K)
10^8
10^6
10^4
10^2
10^0
10^{-2}
10^{-1}
10^0
10^1
10^2
10^3
Gap size (nm)

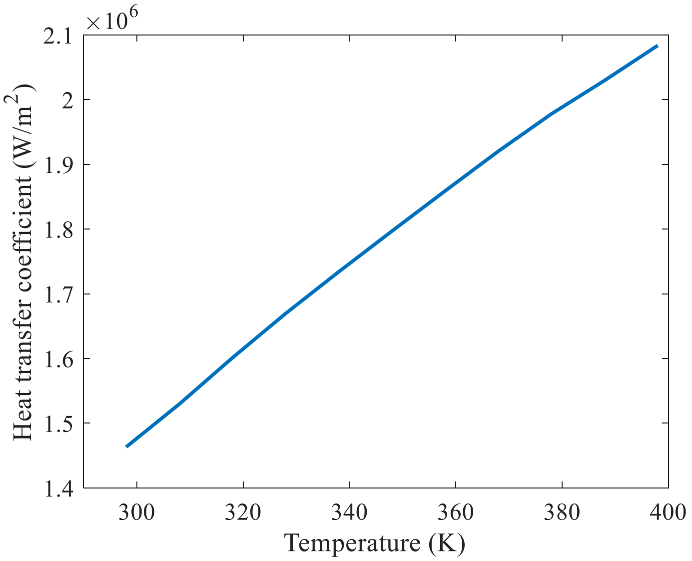
×10^6
Heat transfer coefficient (W/m^2)
2.1
2
1.9
1.8
1.7
1.6
1.5
1.4
300
320
340
360
380
400
Temperature (K)

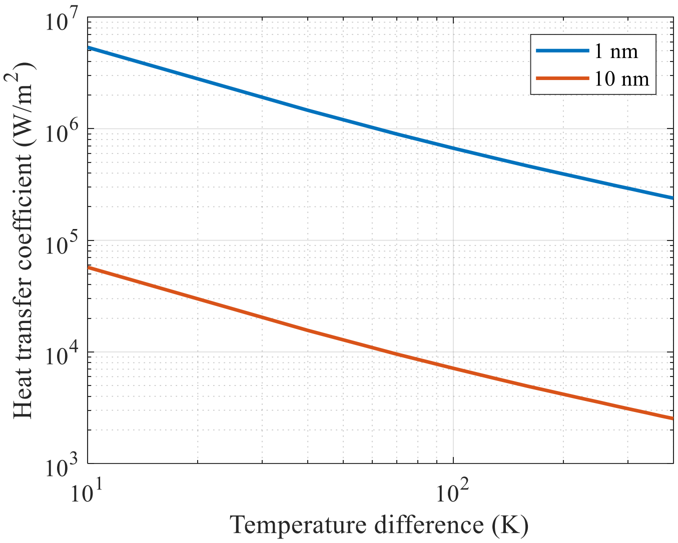

Fig. 4.2.1 Heat transfer coefficient as a function of (a) gap size, (b) temperature of the cold surface and (c) temperature difference

The finite element analysis was performed in the ANSYS APDL platform. On each surface node of the slider, the equivalent heat transfer coefficient is interpolated from its own temperature, the gap size and temperature difference between this node and its counterpart according to Fig. 4.2.1.

To simulate the static touchdown experiment, alumina is chosen as the material of the hot surface and a silicon wafer is the cold surface. Heat sources from both the TFC and TDS are considered in the simulation.

4.3 Finite element modeling and simulation strategy

Finite element analysis is performed in the ANSYS APDL platform and MATLAB. The model consists of two separate geometries: the slider and a small portion of the disk (Fig. 4.3.1). The mesh of the slider is refined at the TFC protrusion area to accurately simulate the deformation and temperature distribution in this region. Another layer of surface elements is modeled on the entire bottom surface of the slider to apply the wave based phonon conduction boundary condition in the form of convection. The surface mesh of the disk contains an area that has identical mesh to the surface mesh on the head. This enables the surface nodes from the head and disk to form node-pairs that will further allow the calculation of heat flux between the disk and head on a node-to-node basis. On the other surfaces of the slider body and the top surface of the disk model, a convection boundary condition of 100 W/(m^{2}K) was applied with the ambient temperature set at 25°C. Since the disk model is large enough, the other surfaces of the disk model are defined with adiabatic boundary condition. Simple-support displacement constraints are applied on the four corners of the bottom surface. The lubricant layer on the disk was ignored in the current analysis.

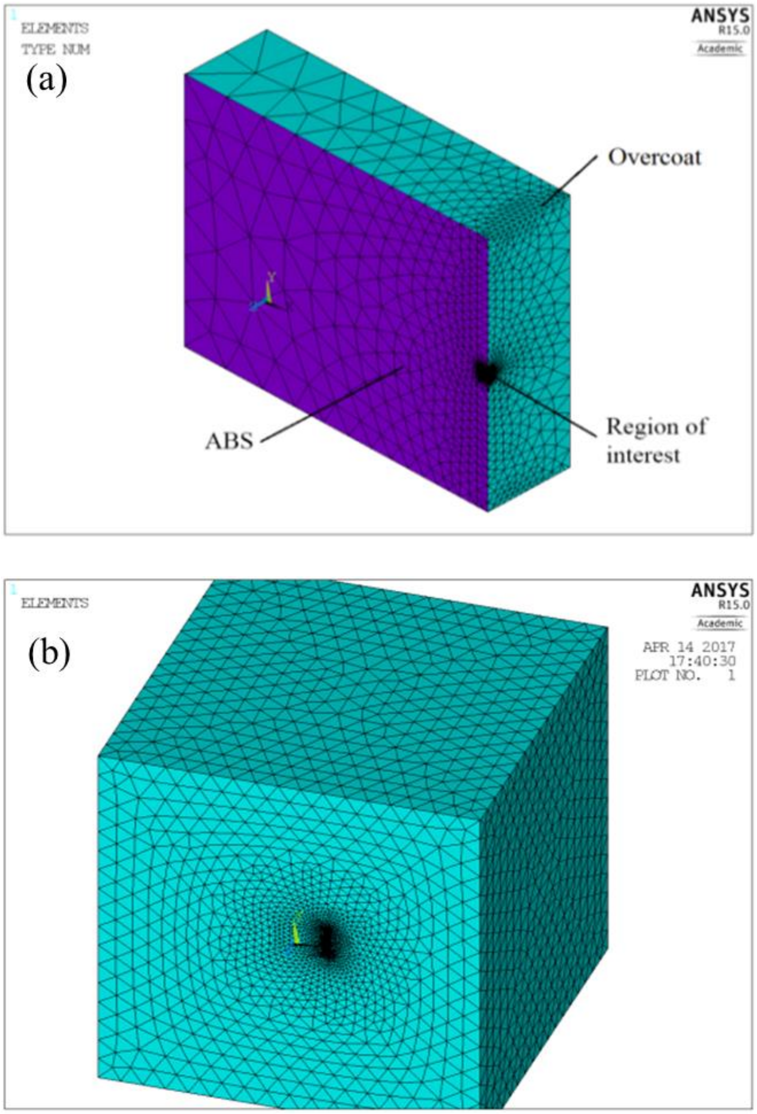

Fig. 4.3.1 Finite element model of (a) the slider and (b) the disk

To simulate the steady state TFC protrusion and temperature of the head, an iteration process is employed to solve the problem in a decoupled sequence on the two geometries while accommodating the wave based phonon conduction boundary condition and providing quick convergence. The simulation process of each given TFC power consists of the following steps (Fig. 4.3.2):

1). On the head model, the initial boundary conditions on all head surfaces are set at free air convection. TFC power and TDS power are applied as heat generation constraints. The initial temperature and deformation are sequentially calculated under this condition.

2). From the initially defined head-disk clearance and the previously calculated TFC protrusion shape, the gap size between each pair of surface nodes is calculated. The heat transfer coefficients between the node-pairs are calculated according to Fig. 4.2.1 with the gap size and temperature difference (T_0 is 25 ^oC at this step).

3). On the disk model, the heat transfer coefficient calculated in step 2) is applied as the boundary condition to calculate the disk temperature profile.

4). According to the disk temperature profile, the equivalent convection heat transfer coefficient is adjusted to keep the heat flux constant.

5). On the slider model, the temperature and deformation is calculated again with the adjusted equivalent convection boundary condition.

6). The deformation of the slider model is saved and steps 2)~5) is repeated until the maximum displacement difference between the two iterations are smaller than the convergence criteria (0.01 nm in this study).

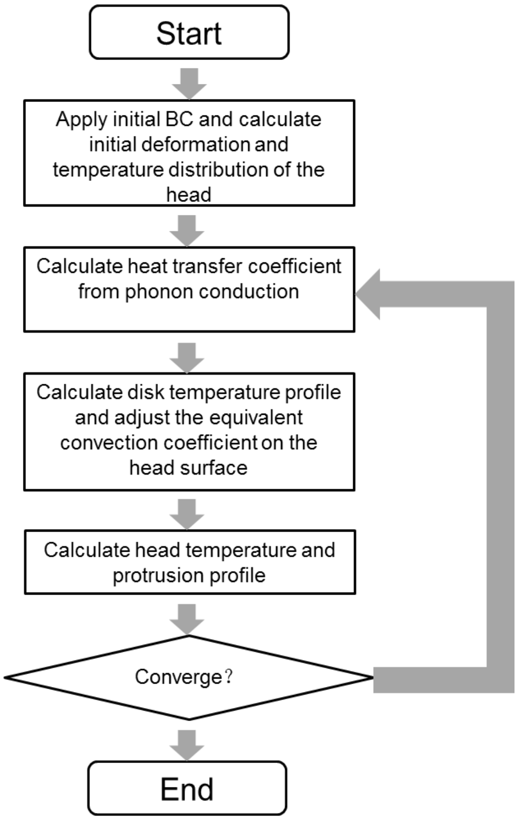

Fig. 4.3.2 Flow chart of the simulation strategy

Since the temperature rise on the disk is much smaller than the head, the deformation of the disk is ignored in this simulation.

To simulate a complete static touchdown experiment curve, a MATLAB script is written to call ANSYS in batch mode and calculate the final TFC protrusion and TDS temperature for each given TFC power.

4.4 Calibration with TFC protrusion profile

To ensure the accuracy of the simulation, the TFC protrusion profile is measured experimentally with Zygo NewView^{TM} 100 interferometer and simulated by ANSYS.

4.4.1 Measurement of TFC protrusion

The Zygo interferometer (Fig. 4.4.1) uses white light coherent scanning interferometry to achieve angstrom level resolution in the z axis. The in-plane resolution differs with the different subject lenses, and with the 40 X subject lens, the resolution in the x and y directions can reach 150 nm. Since the TFC protrusion size is around 20 µm in diameter and the protrusion height is less than 100 nm, the measuring scale of the Zygo fits the purpose perfectly.

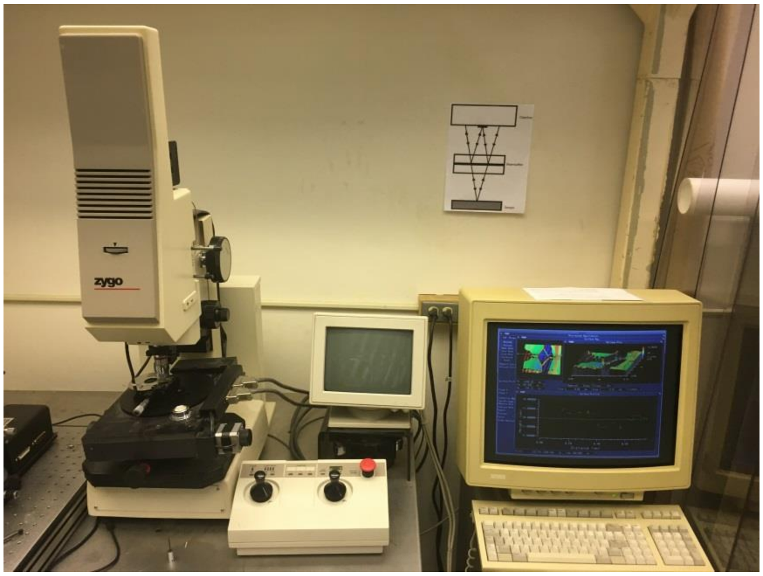

Fig. 4.4.1 Zygo NewView^{TM} 100 observing a PMR slider

The measured TFC protrusion profile at 50 mW TFC power is plotted in Fig. 4.4.2, where the ABS surface feature near the trailing edge center is clearly visible. The TFC protrusion height can be calculate by subtracting the base height from the highest protrusion height. The TFC protrusion height at different TFC powers are plotted and linearly fitted in Fig. 4.4.3. It can be observed that the TFC protrusion rate in air is larger than 0.1 nm/mW.

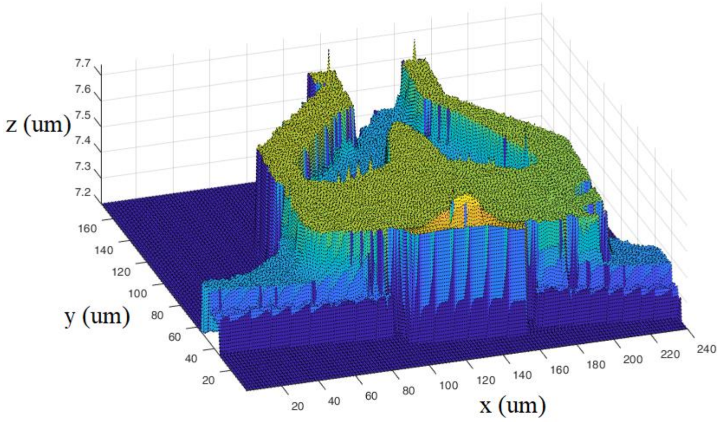

Fig. 4.4.2 TFC protrusion at 50 mW TFC power, measured with Zygo interferometer

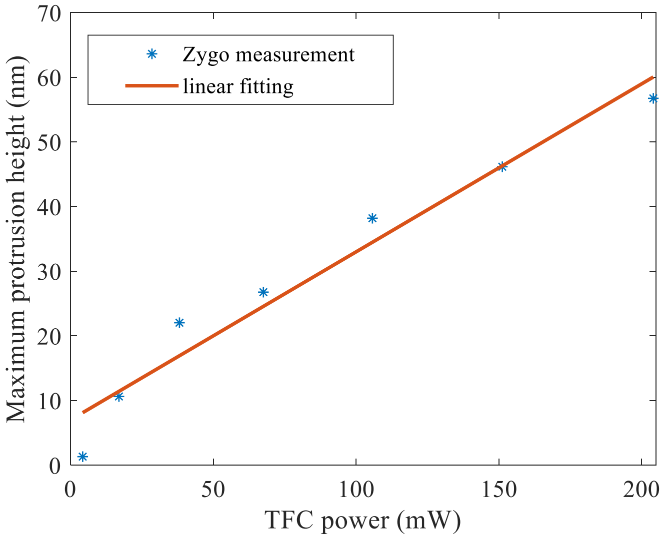

Fig. 4.4.3 Measured TFC protrusion height as a function of TFC power

4.4.2 Simulation of TFC protrusion

A head model is simulated in ANSYS to compare the protrusion shape and protrusion rate with the measured results. The simulated protrusion rate is plotted in Fig. 4.4.4.

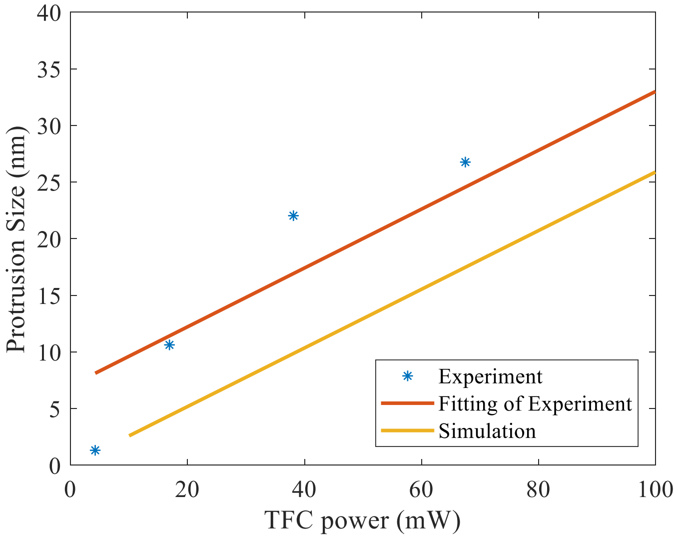

Fig. 4.4.4 Simulate TFC protrusion rate

From Fig. 4.4.4, the fitting of the experimental result within the range of 0 mW to 100 mW is compared with the simulation. The simulated TFC protrusion curve is parallel to the experimentally measured results.

4.5 Results and discussion

4.5.1 Simulation of the static touchdown experiment

The simulation result for a 10 nm initial gap static touchdown experiment is plotted in Fig. 4.5.1. Clearly, the simulation successfully simulated all three stages of the static touchdown experiment. Due to the lack of detailed head design and material properties, there is still some error between the simulation result and the experimental result.

From the simulation, it is also noticeable that the TFC protrusion does not grow linearly with the TFC power during the static touchdown process (Fig. 4.5.2). In Fig. 4.5.2, the first 7 nm TFC protrusion height increase linearly with the TFC power, but when the gap size reduces down to less than 2 nm, the slope of the curve decreases, indicating the increased heat transfer at this scale. This coincides with the drastically increasing heat flux at such a gap size.

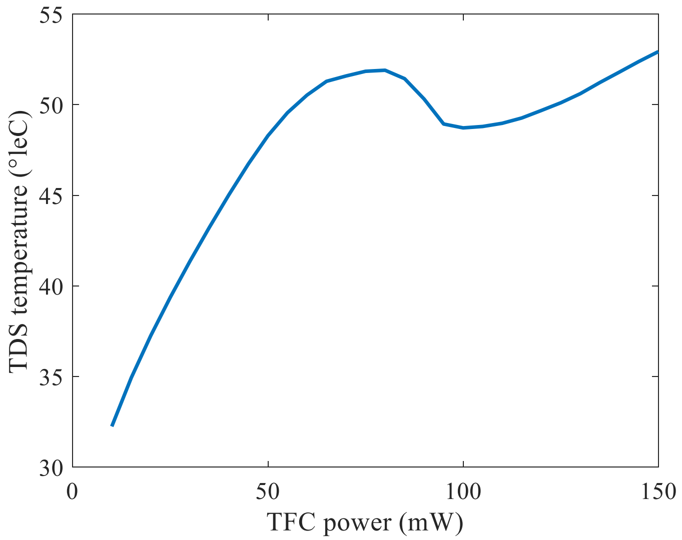

Fig. 4.5.1 Simulated TDS temperature change in a static touchdown process

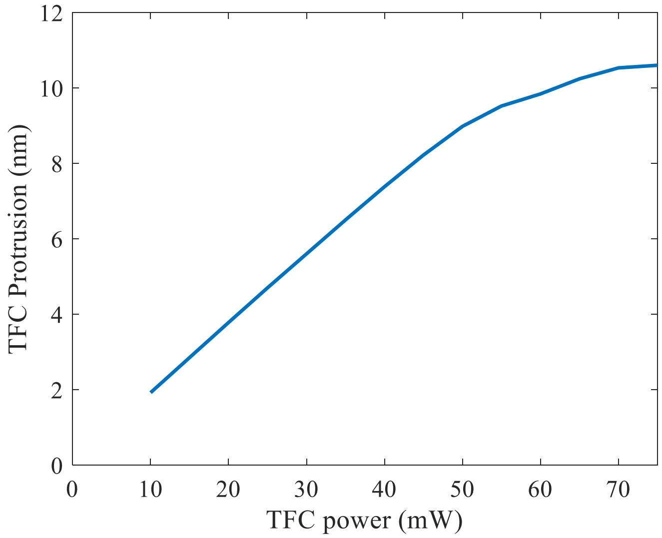

Fig. 4.5.2 TFC Protrusion height as a function of TFC power

The temperature distribution and protrusion shape on the head during the static touchdown experiment are plotted in Fig. 4.5.3.

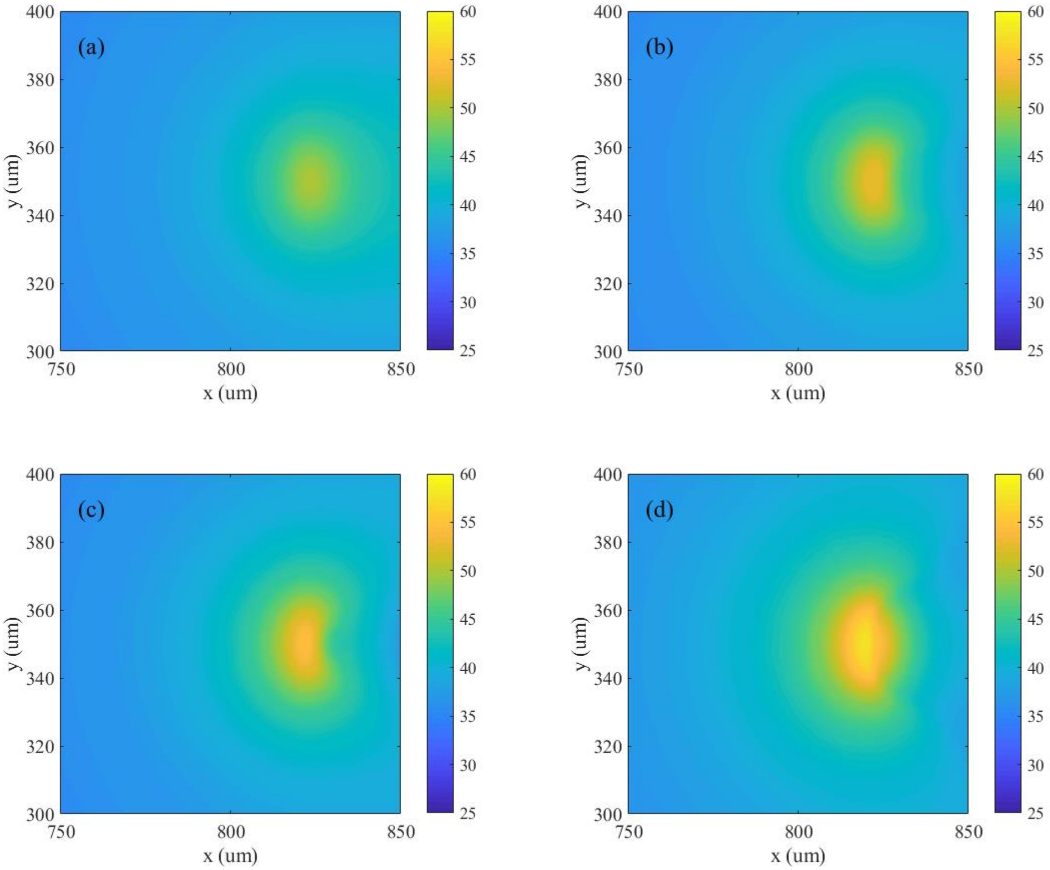

Fig. 4.5.3 Temperature distribution on the head during static touchdown at (a) first heating region, (b) early cooling region, (c) late cooling region and (d) second heating region

According to Fig. 4.5.3, during the first heating region, the temperature profile on the surface of the slider exhibits a Gaussian distribution. However, in the late cooling region, the hottest spot shifts away from the original hottest spot, while the TFC protrusion shape does not change significantly.

4.5.2 Influence of substrate material in static touchdown simulation

Simulations on contact heat transfer with different substrate materials are also performed. The model (Fig. 4.5.4) includes both the head and disk in single geometry. These two bodies are in contact, with a heat resistant layer in between. The simulated results are plotted in Fig. 4.5.5

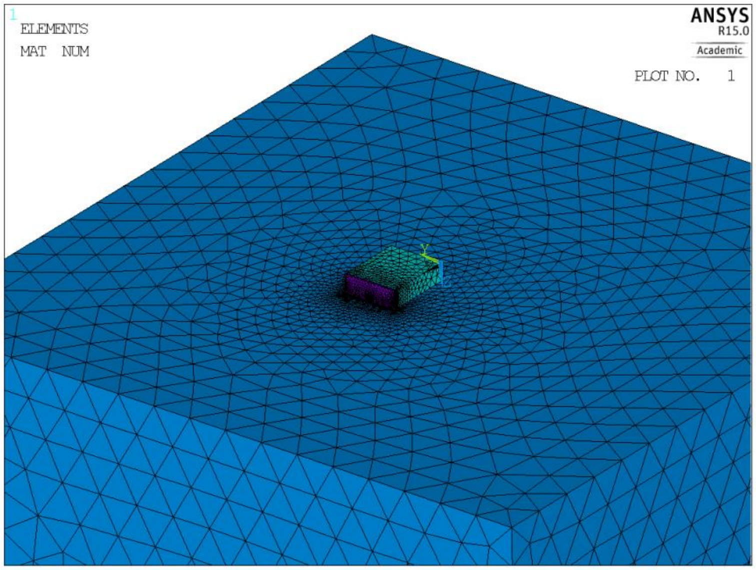

Fig. 4.5.4 Combined head-disk model for contact simulation. Different color represent different materials in the model: Blue region are allocated with disk material properties, purple regions stand for the overcoat of the slider (Al_2O_3) and the green regions are the slider body with Al_2O_3-TiC

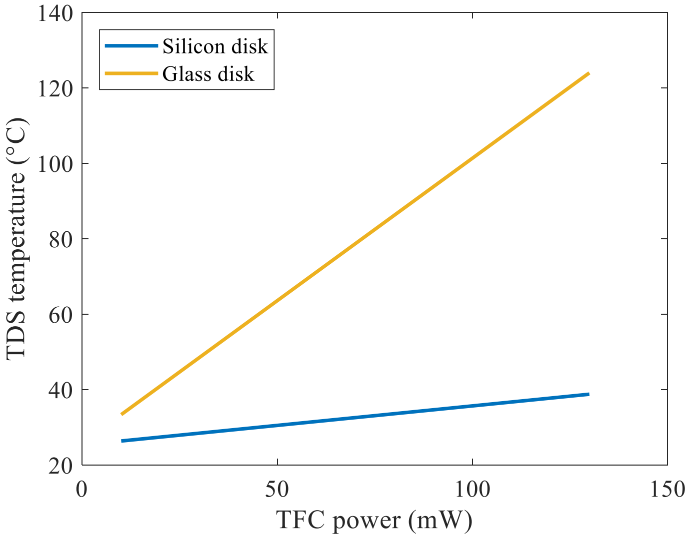

Fig. 4.5.5 Simulated TDS temperature as a function of TFC power at the contact condition with different disk materials

Clearly with disk that has a higher conduction coefficient, the slope of the curve is lower. This simulation further shows the possibility of utilizing the static touchdown experiment as a way to distinguish different disks by conduction coefficient.

The temperature distribution on the disk model is plotted in Fig. 4.5.6. Since the region with temperature elevation on the disk is only less than 200 μm in diameter, this simulation further demonstrates the potential of using the static touchdown experiment as a probe testing method to measuring conduction coefficient on a very small region, since it is only influencing a very small region.

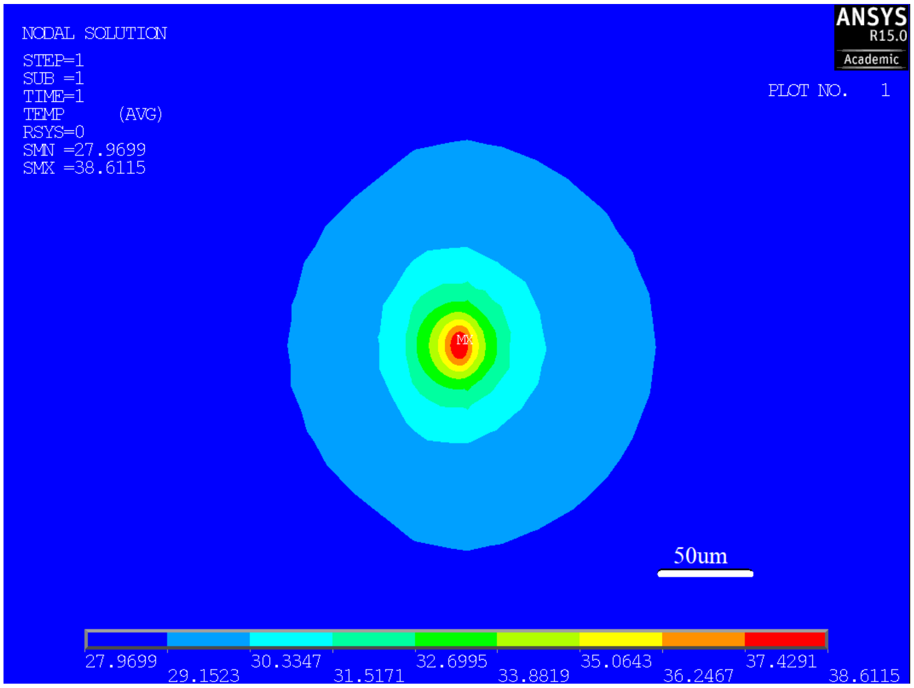

Fig. 4.5.6 Temperature distribution on the disk at contact condition

4.6 Summary and Conclusion

The static touchdown experiment is simulated using wave based phonon conduction theory in ANSYS. The two heating regions and one cooling region in a typical static touchdown experiment are all successfully simulated. The simulation parameters are calibrated with the TFC protrusion shape, which is measured by Zygo white light interferometry. From the simulation, the TFC protrusion height is found to be a non linear function of the TFC power due to increased heat loss to the disk as the gap size reduces. The influence of the substrate is considered and analyzed.

This simulation is the first step towards integrating the wave based phonon conduction theory into the HDI analysis in flying cases and under HAMR conditions.

Chapter 5 Dynamical and thermal response of wave guide heads

5.1 Introduction

As is introduced in Chapter 1, HAMR is the new technology to further boost the areal density of hard disk drives with the help of laser heating. Currently, for HAMR technology, a laser diode is installed on the back of the HAMR head and a beam of laser light shines through the waveguide inside the slider body and onto the NFT. The NFT further focuses the laser spot size down to about 20 nm to locally heat the disk and facilitate magnetic recording [97].

Since the laser travels through the waveguide, part of the energy gets absorbed by the slider body, and it generates unwanted temperature elevation and additional protrusion [86, 87, 98, 99]. These effects can influence the slider's flying stability, and so it needs to be studied carefully [100-102]. However, HAMR heads with the laser diode, waveguide and NFT are not yet available for testing, so a waveguide head, a type of read-write head with the laser diode and waveguide is used in the current setup of experiments. Apart from the NFT, the waveguide heads have identical design and component with normal HAMR heads, and therefore, they are perfect devices for studying laser induced protrusion on the head and dynamical/thermal responses.

In this chapter, the experimental setup and methodology for waveguide head dynamical and thermal transient response measurements are first introduced. Then, the laser diode voltage-ampere characterization are performed to determine the optimum experimental scheme and parameters. Laser induced protrusions at different driving voltages are then measured by use of the touchdown process. Then, the transient dynamical responses of the head-disk interface during laser on/off events are also studied. Finally, the observations from the experiments are summarized.

5.2 Experimental setup

The experimental setup for waveguide head flying testing is similar to the PMR head flying testing setup (Fig. 5.2.1). The mechanical fixture (Fig. 5.2.2) and electrical connection (Fig. 5.2.3) are configured to accommodate the waveguide head.

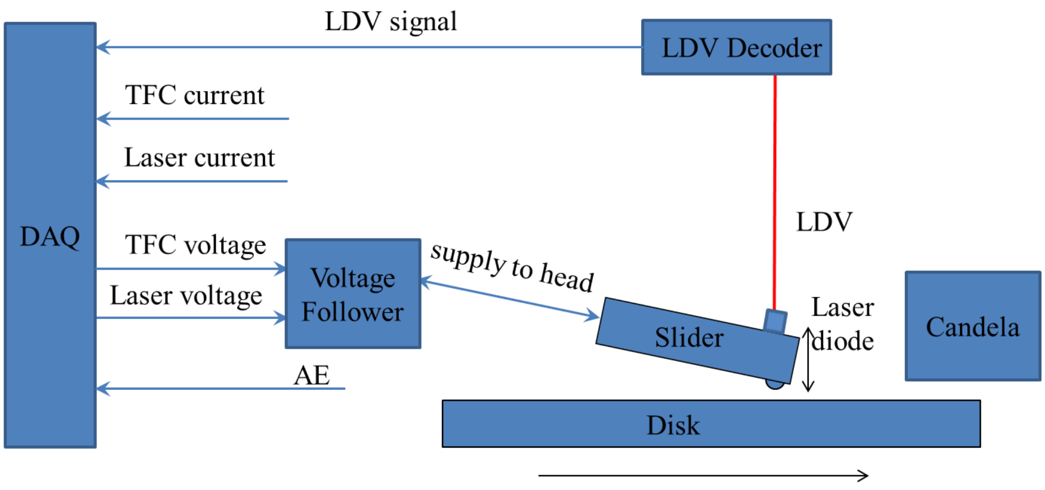

Fig. 5.2.1 Schematic of the experimental setup for the waveguide head

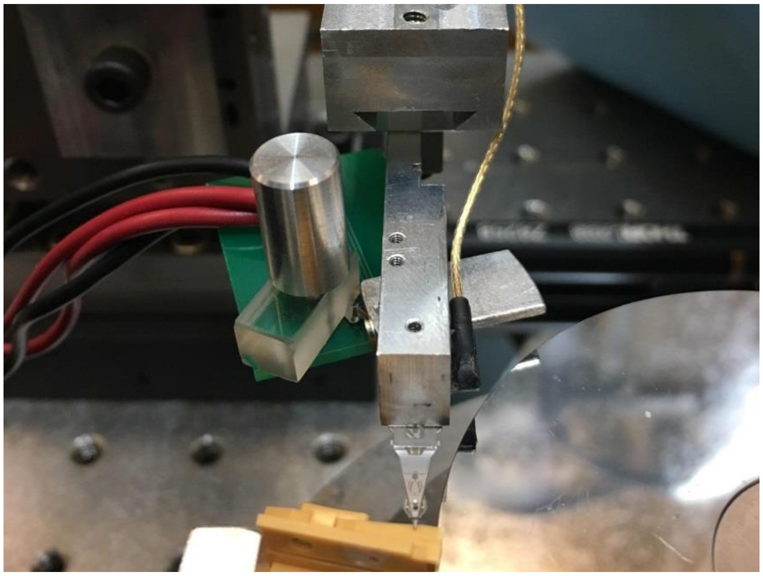

Fig. 5.2.2 Mechanical fixture for the waveguide head

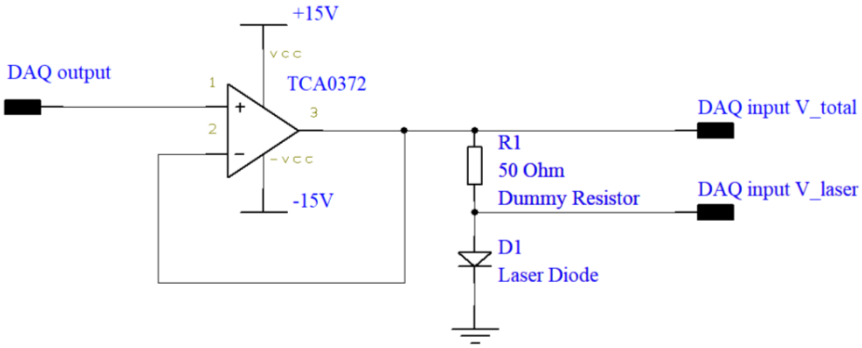

Fig. 5.2.3 Wiring diagram of laser diode connection

Experiments on the waveguide head were performed on the candela OSA spindle at 7200 RPM. The lubricant deformation right after flying the head with their laser on was also recorded. The LDV laser beam is directed onto the back of the laser diode to monitor the trailing edge dynamics of the head, and the AE sensor is used to detect touchdown.

5.3 Methodology

5.3.1 Measurement of laser induced protrusion

While the most direct method of measuring the laser induced protrusion is through profiling measurement including a surface profiler, Zygo interferometer or AFM, these methods each has its own limitations. With a waveguide head, the typical laser power is around 60mW and most of that power is dissipated in the form of laser emission. Therefore, the size of the laser induced protrusion should be much smaller than the TFC protrusion. Therefore, a stylus profiler or Zygo interferometer with micrometer scale lateral resolution is not ideal for this measurement. While the AFM can measure nano-scale features, the laser emitted from the laser diode could affect the detecting laser in the AFM and heat up the AFM tip as well. These factors could affect the accuracy of an AFM measurement and therefore AFM is also not used.

Since the traditional ways of measuring the laser induced protrusion are not applicable here, this protrusion is measured using the TDP decrease method. The assumption of this method is as follows: when the waveguide head is flying on the disk with the laser on, the laser induced protrusion will reduce the clearance between the head and disk. If a touchdown detection process is performed, less TFC power is required to achieve touchdown than in the laser off scenario. Therefore, the decreased amount of TDP reflects the height of the laser induced protrusion. When combined with the measurement results in Chapters 3 and 4, the reliability of the estimation can be improved significantly. Unless otherwise mentioned, the touchdown detections in this chapter are performed in a flying duration of 30 ms.

Since the laser induced protrusion on the disk might also contribute to the TDP decrease, the experiment is conducted on disks with different substrates. Different disk substrates have different material properties including thermal expansion coefficient, conduction coefficient and specific heat capacity. Therefore, the same laser power can induce protrusions of different heights on different disks. If, however, the amounts of TDP decrease on different substrates are identical, this would indicate that the TDP decrease is mostly due to the protrusion on the head.

5.3.2 Evaluation of dynamical response

To evaluate the dynamical response of the head when the laser is turned on suddenly, both LDV signals and AE signals are considered. In this set of experiments, after determining the TDP of the head with laser off, the head is first set to fly at 5 mW back off (TDP - 5mW). Then the laser is turned on and off at a time interval of around 10 ms. The LDV and AE responsees to the laser on/off events are recorded for further analysis.

5.4 Results and discussion

5.4.1 Volt-ampere characteristics of laser diode

Before conducting experiments with wave guide heads, it is necessary to first study the volt-ampere characteristics of the laser diode. The laser diode is connected in series with a standard 50 Ω resistor, and the current running through the laser diode is plotted as a function of V_{total} (Fig. 5.4.1).

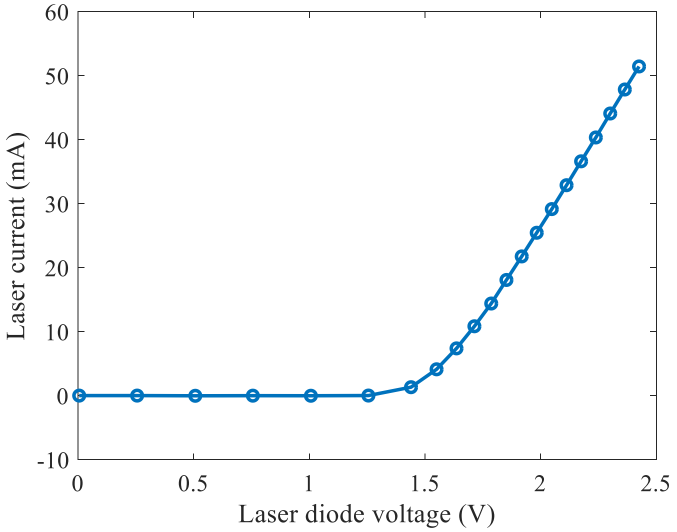

Fig. 5.4.1 The laser current as a function of voltage applied to the laser diode

Fig. 5.4.1 shows that when the voltage applied on the laser diode is less than 1.4 V, the resistance of the laser diode is very high. When the voltage increases beyond 1.4 V, however, the equivalent resistance of the laser diode reduces to around 50 Ω.

While the laser diode is supposed to direct the laser onto the disk, some light leakage can still be observed from the back of the laser diode when the laser is turned on. In Fig. 5.4.2 (a), a bright streak along the side of the laser diode can be observed when the laser is turned on. Through this observation, it is found that 1.4 V is the critical voltage at which the laser is turned on.

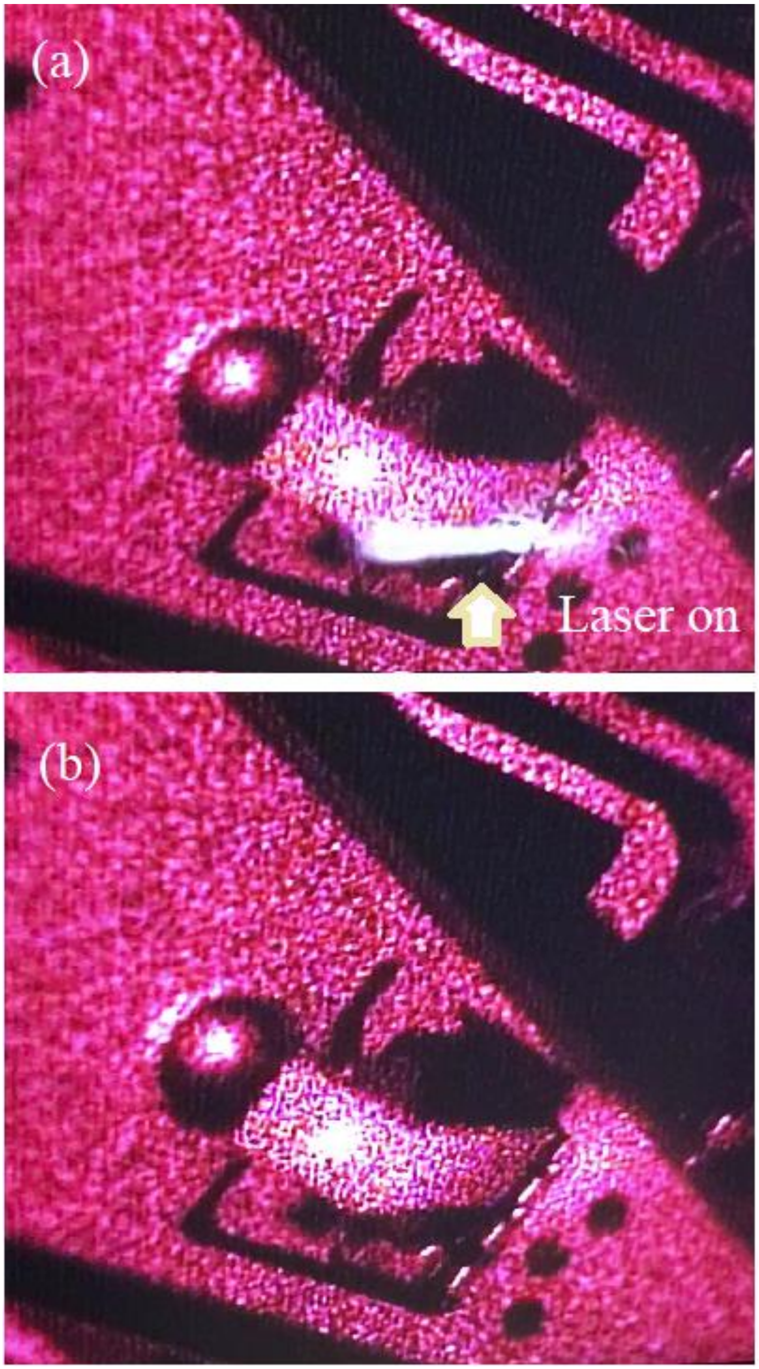

Fig. 5.4.2 Observation of laser diode on and off through a microscope camera: (a) laser on and (b) laser off

5.4.2 Characterization of laser induced protrusion

To study the laser induced protrusion, the TDP decrease effect is measured with the slider flying at the outer radius of a 2.5” PMR disk with glass substrate rotating at 7200 rpm for three times (Fig. 5.4.3)

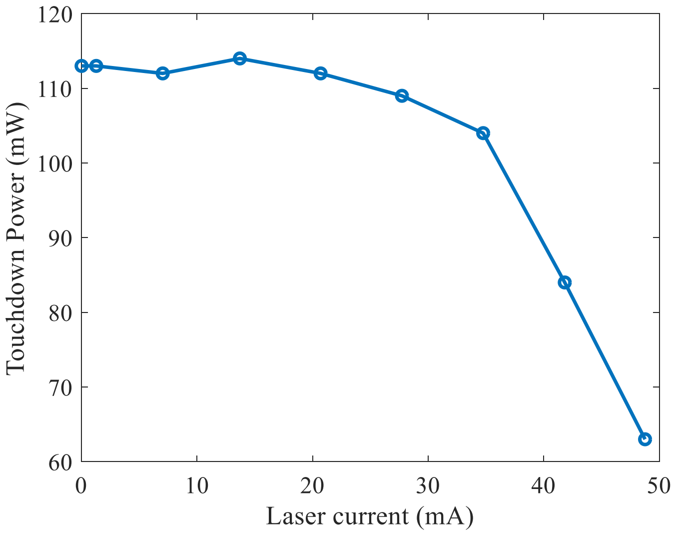

Fig. 5.4.3 TDP decrease of a wave guide head on a PMR disk with a glass substrate

From Fig. 5.4.3, it can be observed that when the laser current is less than 15 mA, the TDP of the head remains almost constant at around 130 mW. As the laser current increases, a more significant TDP decrease can be observed. At 45 mA laser current, the TDP is 10 mW less than the laser off case, because when the laser is off, 10 mW of TFC power corresponds to 1nm of fly height change. Combining this with the simulation results in Chapter 4, the laser induced protrusion at 45 mA is around 1~2nm in height.

To rule out the effect of disk protrusion, the TDP decrease results on glass disks and aluminum disks are compared (Fig. 5.4.4).

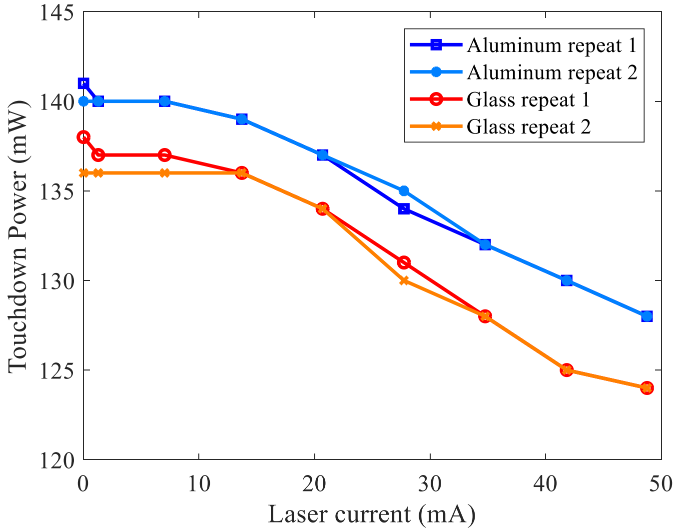

Fig. 5.4.4 TDP decrease of a wave guide head on both glass disk and aluminum disk

In Fig. 5.4.4, it is clear that the TDP decrease curve of the aluminum disk is almost parallel to those of the glass disk. As is discussed in Section 5.3.1, this indicates that the laser induced protrusion on the disk has almost no contribution to the TDP decrease. This is probably because the protrusion on the disk is much smaller or that the protrusions on the head and the disk are not aligned over each other.

The lubricant deformation after flying the wave guide head is measured with a Candela OSA (Fig. 5.4.5). Fig. 5.4.5 shows the reflective index of the disk surface, where the darker regions corresponds to thinner lubricant. It can be observed that moguls form mostly under both the outer and inner edge of the slider. Some moguls or debris and a slight sign of lubricant depletion can also be seen in the center of the track.

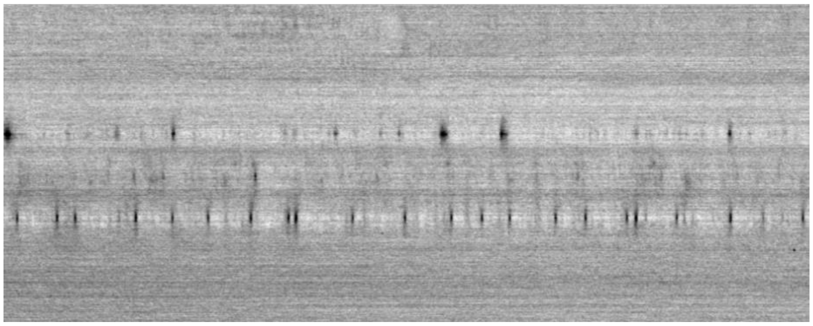

Fig. 5.4.5 Reflective index of the disk surface after flying the wave guide head with laser on

5.4.3 Transient dynamics response of the head disk interface during laser on/off events

While it is clear from Fig. 5.4.3 and Fig. 5.4.4 that TDP decreases when the laser is on, there remains a question as in how long does it take to form the laser induced protrusion. Therefore, another set of experiments were performed. Instead of a touchdown detection duration of 30 ms (4 revolutions of disk rotation), the laser-on time was changed from 2.2 ms to 60 ms. Since each revolution takes 8.3 ms, different starting angle were chosen for cases with 2.2 ms, 4.4 ms and 6.6 ms laser-on detection time.

The results are plotted in Fig. 5.4.6. From this plot, it can be observed that longer laser-on time (60 ms) leads to a slightly larger TDP decrease than shorter laser-on time. The difference between 2.2 ms, 4.4 ms, 6.6 ms, 8.8 ms and 10 ms are not very significant. This indicates that an initial laser-induced protrusion can form within less than 2.2 ms, but it could still develop and protrude more within the next 20 to 40 ms.

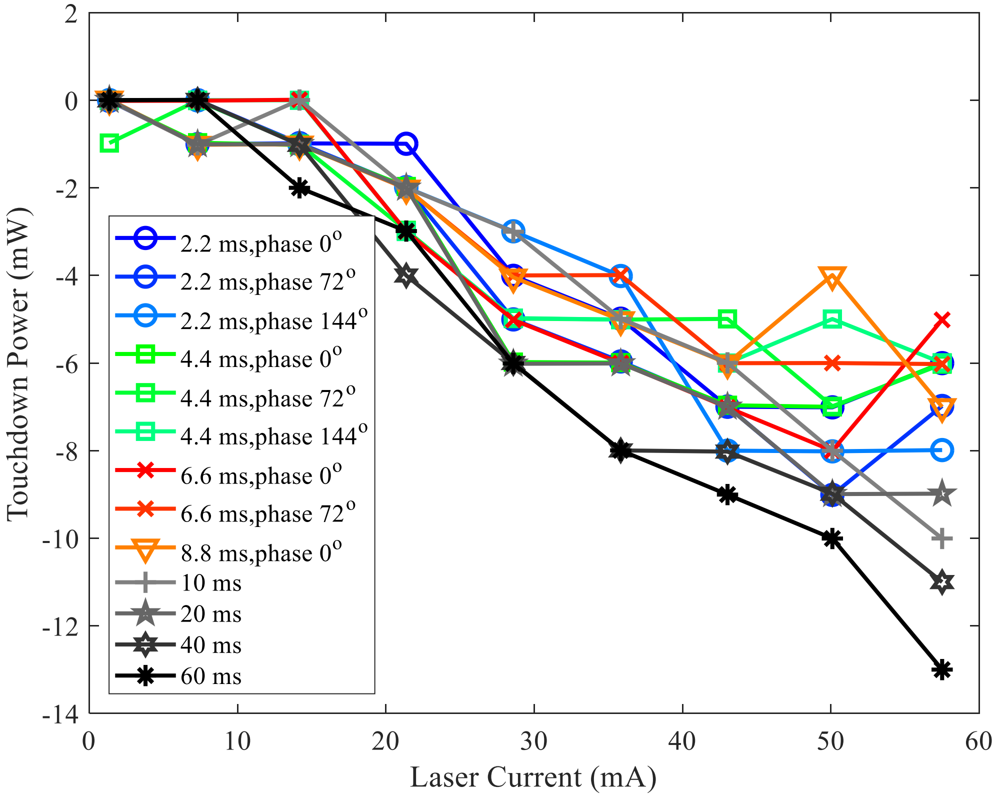

Fig. 5.4.6 TDP decrease with different touchdown duration times

To further study the transient dynamics response of the wave guide head when the laser is turned on, time-frequency analysis of both LDV signal and AE signal are performed. The signals were acquired at different TFC power and laser current (Fig. 5.4.7).

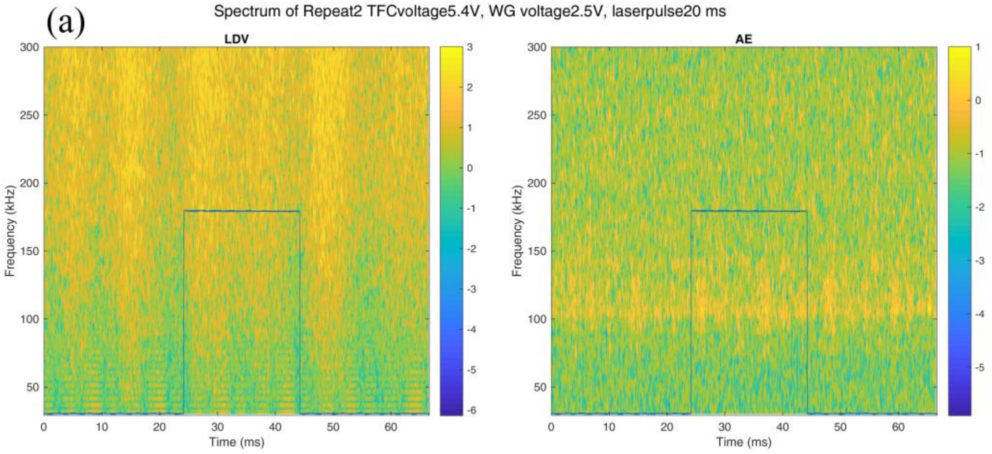

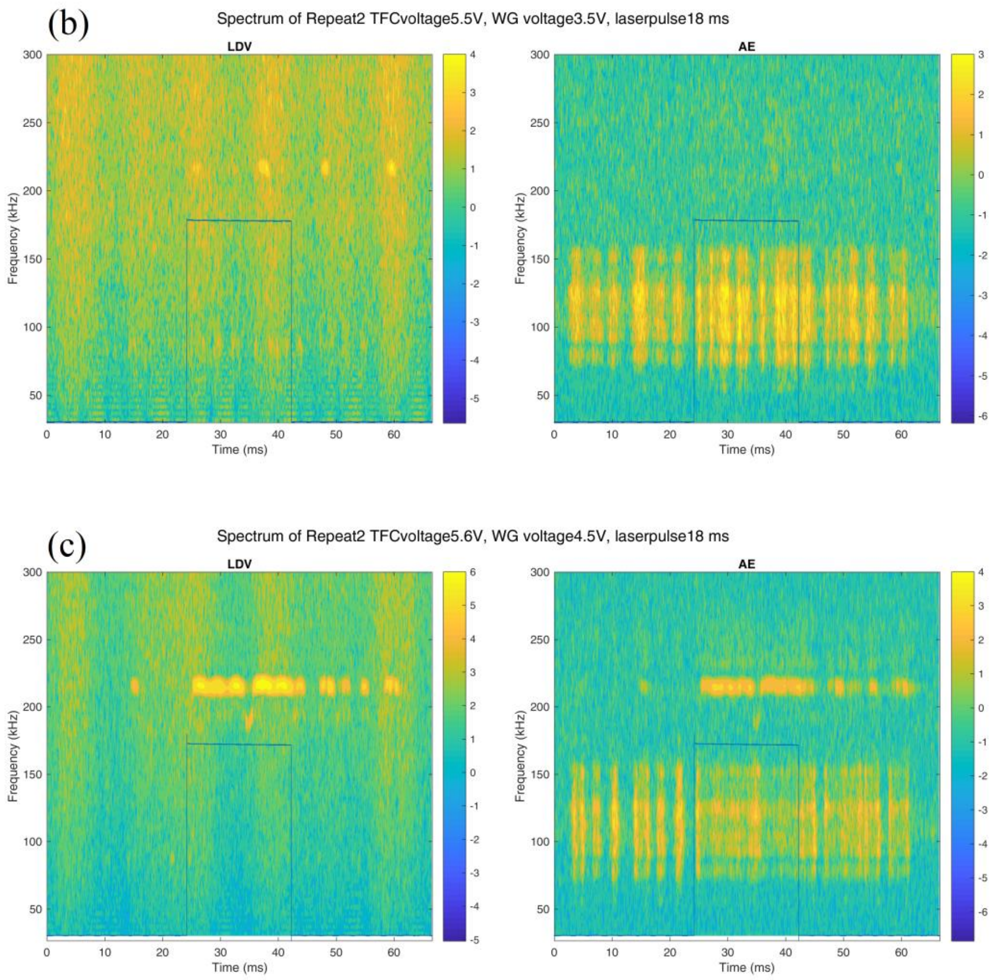

Fig. 5.4.7 Time-frequency analysis of LDV and AE signals for (a) passive flying, (b) contact proximity and (c) heavy over push induced by both TFC and laser power

In Fig. 5.4.7(a), no clear event could be observed from either the LDV or the AE signal, indicating no significant head-disk contact is happening at this stage. In Fig. 5.4.7 (b), a slight signal at 220kHz can be observed in the LDV response around 1 ms after laser-on. These signals can still be observed after turning off the laser, indicating that this contact happens at specific locations on the disk (probably higher peaks), and that the laser might also have induced contamination build-up on the disk, which did not disappear instantly after turning the laser off. At an even higher TFC power and laser current, (Fig. 5.4.7 (c)), head-disk contact changes from point-to-point contact to continuous contact, marked by the continuous band of frequency at 220kHz from both the LDV and AE signals.

To further demonstrate the long-time laser induced protrusion development, another set of experimental results with finer steps of laser current and longer duration of laser power are compared in Fig. 5.4.8. In Fig. 5.4.8 (a), a modulation frequency of 190kHz appears around 8ms after laser turn on, while 210kHz frequency appears around 18ms after turning on the laser. According to the conclusion in Chapter 2, as over push power increases, the modulation frequency should increase. Therefore, this figure demonstrates that laser induced protrusion developed during the 18ms period. When the waveguide voltage is increased slightly from 4.2 V to 4.3 V, strong modulation at 210 kHz can be observed 8ms after turning on the laser. On the other hand, if waveguide voltage is maintained at 4.2 V but TFC voltage is increased to 5.6 V, a continuous, strong signal of contact can be observed at around 8 ms after laser on.

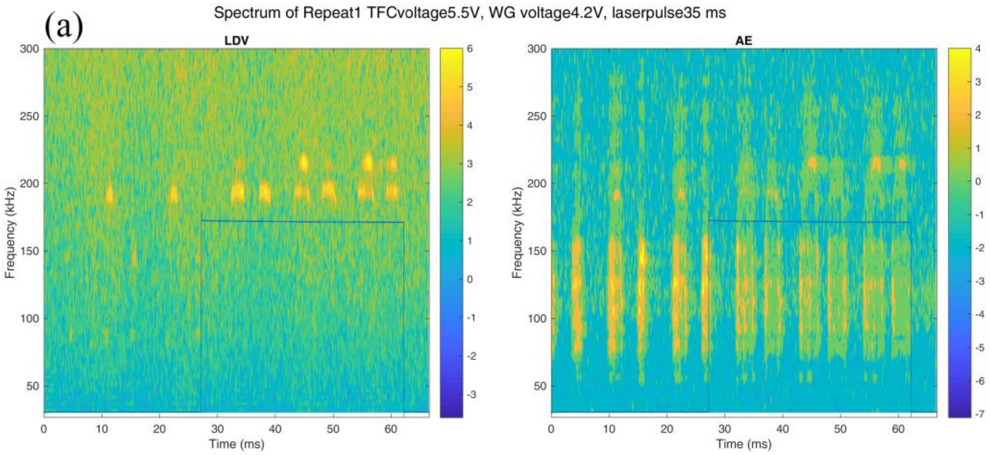

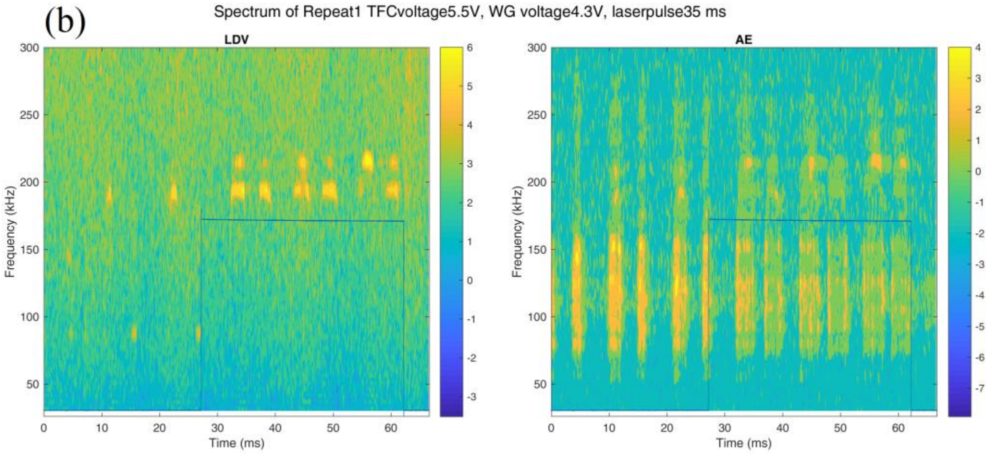

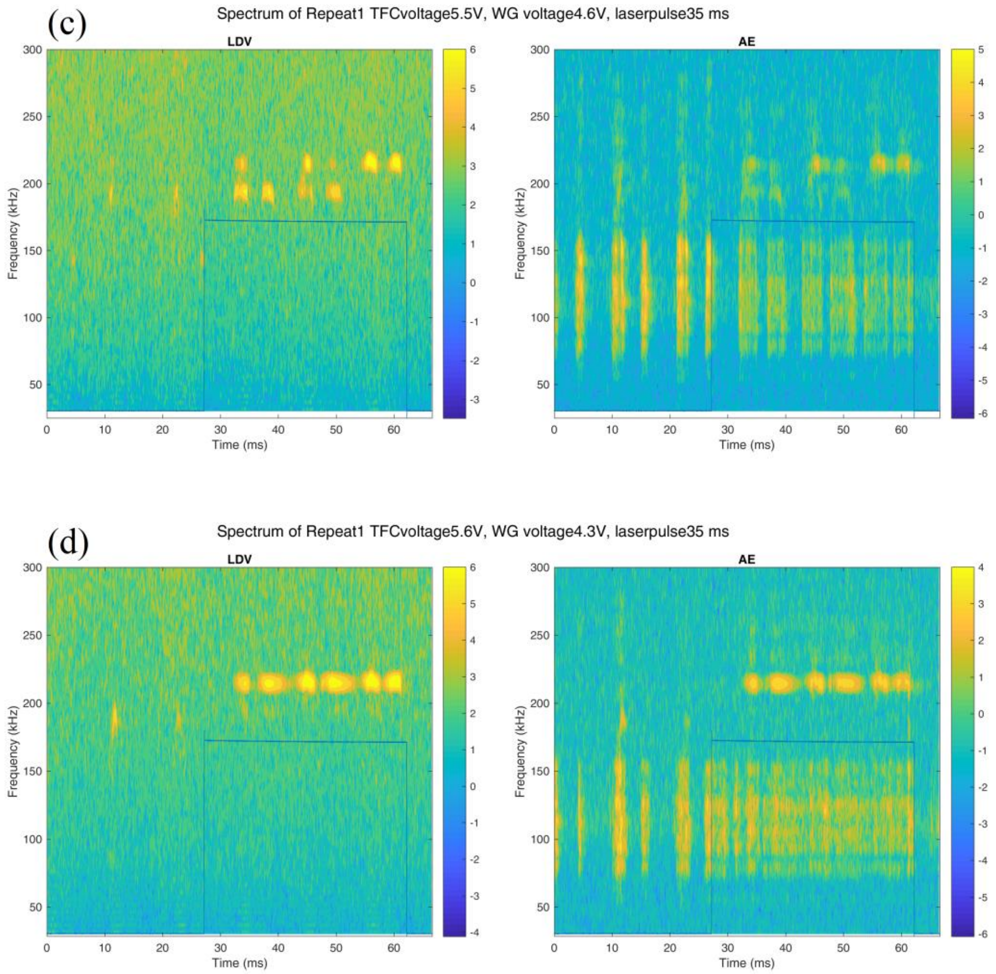

Fig. 5.4.8 Time-frequency analysis of LDV and AE signal contact proximity at different TFC power and laser current

On the basis of Fig. 5.4.7 and Fig. 5.4.8, it is clear that a short time response of the laser induced protrusion can take place within 1ms after turning on the laser, but the protrusion keeps developing over the next 10 to 20 ms. This observation is consistent with the conclusion drawn from Fig. 5.4.6.

5.5 Summary and Conclusion

In this chapter, the experimental setup and methodology for studying the dynamic response of wave guide heads are described. The laser induced protrusion on the wave guide head is measured using the TDP decrease method to be around1~2 nm in height. Comparison between the TDP decrease on disks with different substrates showed that it is not likely to be caused by the protrusion on the disk.

The dynamics of the head disk interface when turning the laser on is also studied. It is found that laser induced protrusion could forms within 1 ms after turning the laser on, but it keeps developing in shape and size over the next 10 to 20 ms. These observations build the foundation for further studies of the dynamics and heat transfer with wave guide heads and HAMR heads.

Chapter 6 Conclusions and future research direction

6.1 Summary

In this dissertation, the dynamics and nano-scale heat transfer behavior in the head disk interface is discussed. Experimental study of nano-scale heat transfer is conducted with a specifically designed static touchdown experiment, and a simulation strategy that incorporates the wave-based phonon conduction theory to simulate the static touchdown experiment was developed. The dynamics of a waveguide head was also studied.

In the flying condition, touchdown experiments were performed at both the drive-level and component-level. During the touchdown process, passive flying, transitional, and modulation stages were identified. More importantly, correlation between the temperature and head disk spacing was found at both the passive flying stage and modulation stage. It was found that when the flying height increases due to either disk surface microwaviness or contact induced modulation, the head temperature also increases, with a slight time delay, indicating the existence of a cooling effect as the head approaches the disk.

By conducting the static touchdown experiment, the nano-scale heat transfer is successfully decoupled from the complicated air flow in the flying condition. The heat transfer behavior across a closing nano-scale gap between the head and disk was observed and measured. Experimental results showed general agreement with the theoretical predictions of the wave based theory for radiation and phonon conduction. The effect of different factors including humidity, air pressure, lubricant layer and disk substrate in the static touchdown experiment were also studied separately.

A simulation method for studying the static touchdown experiment was further developed using the wave based phonon conduction theory in ANSYS and MATLAB. The typical temperature change in a static touchdown experiment was successfully simulated. From the simulation, it was also found that the TFC protrusion height is a nonlinear function of the TFC power due to increased heat loss to the disk as the gap size reduces.

In addition, the dynamics of a waveguide head and its laser induced protrusion was studied. The laser induced protrusion was measured using the TDP decrease method to be around 1~2 nm in height. Comparison between TDP decrease on disks with different substrates showed that this measured TDP decrease is not likely caused by the protrusion on the disk. The dynamics of its HDI when turning the laser on and off was also studied. It was discovered that a fast responding laser induced protrusion forms within 1 ms and a slower responding protrusion forms in the next 10 to 20 ms.

6.2 Future research directions

6.2.1 Experimental study of nano-scale and Angstrom-scale heat transfer

While the static touchdown experiment could achieve heat flux measurement through nano-sized and angstrom-sized gaps, the limited choice of experimental materials (specifically on the head) has made it hard to draw definite conclusions about a near-field heat transfer theory. In a future study, the nano-scale thermal protrusion actuation method in the static touchdown experiment can be improved with microfabrication technology to achieve more reliable results with a wider variety of material choices.

6.2.2 Probing technology of material conduction coefficient and emissivity

The static touchdown experiment has shown its capability of distinguishing different materials by their heat exchange coefficient. Since the diameter of the TFC protrusion is only on the scale of micrometers, this method is capable of measuring heat exchange coefficient on tiny structures such as grains and thin film structures.

6.2.3 Nano-scale heat transfer Simulation of flying condition and HAMR condition

The simulation method introduced in this dissertation can be further improved to simulate the flying condition and HAMR condition. In a flying condition, the variation of head disk spacing can be simulated with CML Air, along with the pressure distribution. Both the air cooling effect and phonon cooling effect can be considered and their contribution to the final head temperature can be compared. In the HAMR condition, the back heating effect can be further included in the model to predict the temperature distribution on the head. These simulation studies should help improve the design of HAMR heads and media.

Bibliography

[1] D. Reinsel, J. Gantz and J. Rydning, '"Data Age 2025: The Evolution of Data to Life-Critical,", vol. 2018, no. April,2017.

[2] B. Marchon, T. Pitchford, Y. Hsia and S. Gangopadhyay, '"The head-disk interface roadmap to an areal density of Tbit/in2," *Advances in Tribology*, vol. 2013,2013.

[3] IBM 350 disk storage unit,https://www-03.ibm.com/ibm/history/exhibits/storage/storage_350.html ,1956.

[4] M. Bohl, '"Introduction to IBM direct access storage devices,", 1981.

[5] 04 de septiembre (1956) IBM lanza el primer disco duro comercial, https://helisulbaran.blogspot.com/2014/09/04-de-septiembre-1956-ibm-lanza-el.html.

[6] A. Chiu, I. Croll, D.E. Heim, R. Jones, P. Kasiraj, K.B. Klaassen, C.D. Mee and R.G. Simmons, '"Thin-film inductive heads," *IBM journal of research and development*, vol. 40, no. 3, pp. 283-300,1996.

[7] C. Tsang, T. Lin, S. MacDonald, M. Pinarbasi, N. Robertson, H. Santini, M. Doerner, T. Reith, L. Vo and T. Diola, '"5 Gb/in/sup 2/recording demonstration with conventional AMR dual element heads and thin film disks," *IEEE Trans.Magn.*, vol. 33, no. 5, pp. 2866-2871,1997.

[8] M.N. Baibich, J.M. Broto, A. Fert, F.N. Van Dau, F. Petroff, P. Etienne, G. Creuzet, A. Friederich and J. Chazelas, '"Giant magnetoresistance of (001) Fe/(001) Cr magnetic superlattices," *Phys.Rev.Lett.*, vol. 61, no. 21, pp. 2472,1988.

[9] P.M. Levy, '"Giant magnetoresistance in magnetic layered and granular materials," *Science*, vol. 256, no. 5059, pp. 972-974,1992.

[10] S. Iwasaki, '"Perpendicular magnetic recording," *IEEE Trans.Magn.*, vol. 16, no. 1, pp. 71-76,1980.

[11] S. Khizroev and D. Litvinov, '"Perpendicular magnetic recording,", 2006.

[12] P.E. Kupinski, J.C. Liu and D.W. Meyer, '"Slider with temperature responsive transducer positioning," *Slider with temperature responsive transducer positioning*,1999.

[13] D. Meyer, Z. Boutaghou and B. Wei, '"Proximity recording-the concept of self-adjusting fly heights," *IEEE Trans.Magn.*, vol. 33, no. 1, pp. 912-917,1997.

[14] N. Liu, J. Zheng and D.B. Bogy, '"Thermal flying-height control sliders in hard disk drives filled with air-helium gas mixtures," *Appl.Phys.Lett.*, vol. 95, no. 21, pp. 213505,2009.

[15] R. Wood, '"Future hard disk drive systems," *J Magn Magn Mater*, vol. 321, no. 6, pp. 555-561,2009.

[16] J. Yang, C.P.H. Tan and E.H. Ong, '"Thermal analysis of helium-filled enterprise disk drive," *Microsystem technologies*, vol. 16, no. 10, pp. 1699-1704,2010.

[17] J.E. Jacoby and J.R. Gustafson, *Disk drive having a conformal laminated cover seal adhered a top face and four side faces of a helium-filled enclosure*,2011.

[18] A. Amer, J. Holliday, D.D. Long, E.L. Miller, J. Pâris and T. Schwarz, '"Data management and layout for shingled magnetic recording," *IEEE Trans.Magn.*, vol. 47, no. 10, pp. 3691-3697,2011.

[19] T. Feldman and G. Gibson, '"Shingled magnetic recording: Areal density increase requires new data management," *USENIX; login: Magazine*, vol. 38, no. 3,2013.

[20] M.H. Kryder, E.C. Gage, T.W. McDaniel, W.A. Challener, R.E. Rottmayer, G. Ju, Y. Hsia and M.F. Erden, '"Heat assisted magnetic recording," *Proc IEEE*, vol. 96, no. 11, pp. 1810-1835,2008.

[21] J. Zhu, X. Zhu and Y. Tang, '"Microwave assisted magnetic recording," *IEEE Trans.Magn.*, vol. 44, no. 1, pp. 125-131,2008.

[22] J. Zhu and Y. Wang, '"Microwave assisted magnetic recording utilizing perpendicular spin torque oscillator with switchable perpendicular electrodes," *IEEE Trans.Magn.*, vol. 46, no. 3, pp. 751-757,2010.

[23] R. Wood, M. Williams, A. Kavcic and J. Miles, '"The feasibility of magnetic recording at 10 terabits per square inch on conventional media," *IEEE Trans.Magn.*, vol. 45, no. 2, pp. 917-923,2009.

[24] K.S. Chan, R. Radhakrishnan, K. Eason, M.R. Elidrissi, J.J. Miles, B. Vasic and A.R. Krishnan, '"Channel models and detectors for two-dimensional magnetic recording," *IEEE Trans.Magn.*, vol. 46, no. 3, pp. 804-811,2010.

[25] E. Hwang, R. Negi and B.V. Kumar, '"Signal processing for near 10 Tbit/in $^{2} $ density in two-dimensional magnetic recording (TDMR)," *IEEE Trans.Magn.*, vol. 46, no. 6, pp. 1813-1816,2010.

[26] T.R. Albrecht, H. Arora, V. Ayanoor-Vitikkate, J. Beaujour, D. Bedau, D. Berman, A.L. Bogdanov, Y. Chapuis, J. Cushen and E.E. Dobisz, '"Bit-patterned magnetic recording: Theory, media fabrication, and recording performance," *IEEE Trans.Magn.*, vol. 51, no. 5, pp. 1-42,2015.

[27] O. Hellwig, J. Bosworth, E. Dobisz, D. Kercher, T. Hauet, G. Zeltzer, J. Risner-Jamtgaard, D. Yaney and R. Ruiz, '"Bit patterned media based on block copolymer directed assembly with narrow magnetic switching field distribution," *Appl.Phys.Lett.*, vol. 96, no. 5, pp. 052511,2010.

[28] H. Richter, A. Dobin, R. Lynch, D. Weller, R. Brockie, O. Heinonen, K. Gao, J. Xue, R.v. Veerdonk and P. Asselin, '"Recording potential of bit-patterned media," *Appl.Phys.Lett.*, vol. 88, no. 22, pp. 222512,2006.

[29] Q. Zeng, B.H. Thornton, D.B. Bogy and C.S. Bhatia, '"Flyability and flying height modulation measurement of sliders with sub-10 nm flying heights," *IEEE Trans.Magn.*, vol. 37, no. 2, pp. 894-899,2001.

[30] J. Juang, D. Chen and D.B. Bogy, '"Alternate air bearing slider designs for areal density of 1 Tb/in/sup 2," *IEEE Trans.Magn.*, vol. 42, no. 2, pp. 241-246,2006.

[31] Y. Shimizu, J. Xu, H. Kohira, M. Kurita, T. Shiramatsu and M. Furukawa, '"Nano-scale defect mapping on a magnetic disk surface using a contact sensor," *Magnetics, IEEE Transactions on*, vol. 47, no. 10, pp. 3426-3432,2011.

[32] J. Li, J. Xu, J. Liu and H. Kohira, '"Thermal mechanics of a contact sensor used in hard disk drives," *Microsystem technologies*, vol. 19, no. 9-10, pp. 1607-1614,2013.

[33] W. Challener, C. Peng, A. Itagi, D. Karns, W. Peng, Y. Peng, X. Yang, X. Zhu, N. Gokemeijer and Y. Hsia, '"Heat-assisted magnetic recording by a near-field transducer with efficient optical energy transfer," *Nature photonics*, vol. 3, no. 4, pp. 220,2009.

[34] B.C. Stipe, T.C. Strand, C.C. Poon, H. Balamane, T.D. Boone, J.A. Katine, J. Li, V. Rawat, H. Nemoto and A. Hirotsune, '"Magnetic recording at 1.5 Pb m− 2 using an integrated plasmonic antenna," *Nature photonics*, vol. 4, no. 7, pp. 484,2010.

[35] S. Bhargava and E. Yablonovitch, '"Lowering HAMR near-field transducer temperature via inverse electromagnetic design," *IEEE Trans.Magn.*, vol. 51, no. 4, pp. 1-7,2015.

[36] H. Tani, Y. Uesaraie, R. Lu, S. Koganezawa and N. Tagawa, '"Smear growth on head slider surface from siloxane outgas on heat assisted magnetic recording," *Microsystem Technologies*, pp. 1-8.

[37] S.V. Sakhalkar and D.B. Bogy, '"A Model for Lubricant Transfer from Media to Head During Heat-Assisted Magnetic Recording (HAMR) Writing," *Tribology Letters*, vol. 65, no. 4, pp. 166,2017.

[38] B.V. Budaev and D.B. Bogy, '"Computation of radiative heat transport across a nanoscale vacuum gap," *Appl.Phys.Lett.*, vol. 104, no. 6, pp. 061109,2014.

[39] B.V. Budaev and D.B. Bogy, '"Heat transport by phonon tunneling across layered structures used in heat assisted magnetic recording," *J.Appl.Phys.*, vol. 117, no. 10, pp. 104512,2015.

[40] B.V. Budaev and D.B. Bogy, '"A self-consistent acoustics model of interface thermal resistance," *SIAM J Appl Math*, vol. 70, no. 5, pp. 1691-1710,2010.

[41] B.V. Budaev and D.B. Bogy, '"An extension of Khalatnikov's theory of Kapitsa thermal resistance," *Annalen der Physik*, vol. 523, no. 3, pp. 208-225,2011.

[42] B.V. Budaev and D.B. Bogy, '"Extension of Planck's law of thermal radiation to systems with a steady heat flux," *Annalen der Physik*, vol. 523, no. 10, pp. 791-804,2011.

[43] J. Juang, J. Forrest and F. Huang, '"Magnetic head protrusion profiles and wear pattern of thermal flying-height control sliders with different heater designs," *IEEE Trans.Magn.*, vol. 47, no. 10, pp. 3437-3440,2011.

[44] Y. Shimizu, J. Xu, H. Kohira, K. Kuroki and K. Ono, '"Experimental study on slider dynamics during touchdown by using thermal flying-height control," *Microsystem technologies*, vol. 17, no. 5-7, pp. 897-902,2011.

[45] T. Shiramatsu, T. Atsumi, M. Kurita, Y. Shimizu and H. Tanaka, '"Dynamically controlled thermal flying-height control slider," *IEEE Trans.Magn.*, vol. 44, no. 11, pp. 3695-3697,2008.

[46] J. Zheng and D.B. Bogy, '"Investigation of flying-height stability of thermal fly-height control sliders in lubricant or solid contact with roughness," *Tribology letters*, vol. 38, no. 3, pp. 283-289,2010.

[47] Y. Chen, J. Peng and D.B. Bogy, '"Thermal protrusion-induced air bearing slider instability at disk proximity and light contact," *IEEE Trans.Magn.*, vol. 50, no. 7, pp. 1-7,2014.

[48] S.V. Canchi and D.B. Bogy, '"Slider dynamics in the lubricant-contact regime," *Magnetics, IEEE Transactions on*, vol. 46, no. 3, pp. 764-769,2010.

[49] Y. Chen, J. Zheng and D.B. Bogy, '"Light contact and surfing state dynamics of air bearing sliders in hard disk drives," *Appl.Phys.Lett.*, vol. 100, no. 24, pp. 243104,2012.

[50] Y. Chen, J. Peng and D.B. Bogy, '"Thermal Protrusion-Induced Air Bearing Slider Instability at Disk Proximity and Light Contact," *IEEE Trans.Magn.*, vol. 50, no. 7, pp. 3301707,2014.

[51] Y. Ma, S. Xue, J. Peng and D.B. Bogy, '"Study of head-disk interface characterization using touchdown sensor and electromagnetic signal in hard disk drives," *IEEE Trans.Magn.*, vol. 51, no. 11, pp. 1-4,2015.

[52] A. Daugela and S. Tadepalli, '"Drive level acoustic defectoscopy for head disc interface (HDI) integration and manufacturing," *Microsystem technologies*, vol. 18, no. 9-10, pp. 1425-1430,2012.

[53] J. Xu, Y. Shimizu and L. Su, '"Drive level measurement of flying height modulation and control of slider disk contact,", pp. 869-873,2006.

[54] J. Li, J. Xu, J. Liu and H. Kohira, '"Thermal mechanics of a contact sensor used in hard disk drives," *Microsystem technologies*, vol. 19, no. 9-10, pp. 1607-1614,2013.

[55] J. Liu, J. Xu and J. Li, '"Simulation studies of contact sensor for disk defect mapping," *Microsystem technologies*, vol. 19, no. 9-10, pp. 1441-1448,2013.

[56] J. Xu, Y. Shimizu, J. Liu, T. Shiramatsu, M. Furukawa, J. Li and H. Kohira, '"Pit detection using a contact sensor," *Magnetics, IEEE Transactions on*, vol. 49, no. 6, pp. 2715-2718,2013.

[57] J. Xu, Y. Shimizu, M. Furukawa, J. Li, Y. Sano, T. Shiramatsu, Y. Aoki, H. Matsumoto, K. Kuroki and H. Kohira, '"Contact/Clearance Sensor for HDI Subnanometer Regime," *Magnetics, IEEE Transactions on*, vol. 50, no. 3, pp. 114-118,2014.

[58] X. Ma, J. Chen, H.J. Richter, H. Tang and J. Gui, '"Contribution of lubricant thickness to head-media spacing," *IEEE Trans.Magn.*, vol. 37, no. 4, pp. 1824-1826,2001.

[59] Z. Yuan, B. Liu, W. Zhang and S. Hu, '"Engineering study of triple-harmonic method for in situ characterization of head–disk spacing," *J Magn Magn Mater*, vol. 239, no. 1, pp. 367-370,2002.

[60] Y. Chen, J. Peng and D.B. Bogy, '"Thermal protrusion-induced air bearing slider instability at disk proximity and light contact," *Magnetics, IEEE Transactions on*, vol. 50, no. 7, pp. 1-7,2014.

[61] R. Chen, M. Lu, V. Srinivasan, Z. Wang, H.H. Cho and A. Majumdar, '"Nanowires for enhanced boiling heat transfer," *Nano letters*, vol. 9, no. 2, pp. 548-553,2009.

[62] G. Chen, '"Nanoscale heat transfer and nanostructured thermoelectrics,", vol. 1, pp. 8-17,2004.

[63] E. Rousseau, A. Siria, G. Jourdan, S. Volz, F. Comin, J. Chevrier and J. Greffet, '"Radiative heat transfer at the nanoscale," *Nature Photonics*, vol. 3, no. 9, pp. 514-517,2009.

[64] J.J. Vadasz, S. Govender and P. Vadasz, '"Heat transfer enhancement in nano-fluids suspensions: possible mechanisms and explanations," *Int.J.Heat Mass Transfer*, vol. 48, no. 13, pp. 2673-2683,2005.

[65] A. Zaluska, L. Zaluski and J. Ström-Olsen, '"Structure, catalysis and atomic reactions on the nano-scale: a systematic approach to metal hydrides for hydrogen storage," *Applied Physics A*, vol. 72, no. 2, pp. 157-165,2001.

[66] Y. Ma, A. Ghafari, B. Budaev and D. Bogy, '"Controlled heat flux measurement across a closing nanoscale gap and its comparison to theory," *Appl.Phys.Lett.*, vol. 108, no. 21, pp. 213105,2016.

[67] Y. Ma, A. Ghafari, B.V. Budaev and D.B. Bogy, '"Measurement and simulation of nanoscale gap heat transfer using a read/write head with a contact sensor," *IEEE Trans.Magn.*, vol. 53, no. 2, pp. 1-5,2017.

[68] Y. Ma and D.B. Bogy, '"Experimental Investigation of Heat Flux at the Head-Disk Interface in Hard Disk Drives,", pp. V001T01A008-V001T01A008,2016.

[69] M. Planck, '"The theory of heat radiation,", 1914.

[70] S.M. Rytov, '"Theory of electrical fluctuations and thermal radiation,", 1959.

[71] S.M. Rytov, Y.A. Kravtsov and V. Tatarskii, '"Elements of random fields," *Principles of Statistical Radiophysics*, vol. vol 3,1989.

[72] D. Polder and M. Van Hove, '"Theory of radiative heat transfer between closely spaced bodies," *Physical Review B*, vol. 4, no. 10, pp. 3303,1971.

[73] P. Kapitza, '"The study of heat transfer in helium II," *J.Phys.(USSR)*, vol. 4, no. 1-6, pp. 181-210,1941.

[74] S. Shen, A. Narayanaswamy and G. Chen, '"Surface phonon polaritons mediated energy transfer between nanoscale gaps," *Nano letters*, vol. 9, no. 8, pp. 2909-2913,2009.

[75] B. Song, Y. Ganjeh, S. Sadat, D. Thompson, A. Fiorino, V. Fernández-Hurtado, J. Feist, F.J. Garcia-Vidal, J.C. Cuevas and P. Reddy, '"Enhancement of near-field radiative heat transfer using polar dielectric thin films," *Nature nanotechnology*, vol. 10, no. 3, pp. 253-258,2015.

[76] B. Song, A. Fiorino, E. Meyhofer and P. Reddy, '"Near-field radiative thermal transport: From theory to experiment," *AIP Advances*, vol. 5, no. 5, pp. 053503,2015.

[77] K. Kim, B. Song, V. Fernández-Hurtado, W. Lee, W. Jeong, L. Cui, D. Thompson, J. Feist, M.H. Reid and F.J. García-Vidal, '"Radiative heat transfer in the extreme near field," *Nature*,2015.

[78] D.B. Asay and S.H. Kim, '"Effects of adsorbed water layer structure on adhesion force of silicon oxide nanoasperity contact in humid ambient," *J.Chem.Phys.*, vol. 124, no. 17, pp. 174712,2006.

[79] Y. Li, D. Trauner and F. Talke, '"Effect of humidity on stiction and friction of the head/disk interface," *IEEE Trans.Magn.*, vol. 26, no. 5, pp. 2487-2489,1990.

[80] H. Tian and T. Matsudaira, '"The role of relative humidity, surface roughness and liquid build-up on static friction behavior of the head/disk interface," *Journal of tribology*, vol. 115, no. 1, pp. 28-35,1993.

[81] Y. Ma, A. Ghafari, B. Budaev and D. Bogy, '"Controlled heat flux measurement across a closing nanoscale gap and its comparison to theory," *Appl.Phys.Lett.*, vol. 108, no. 21, pp. 213105,2016.

[82] B.V. Budaev and D.B. Bogy, '"On thermal radiation across nanoscale gaps," *Zeitschrift für angewandte Mathematik und Physik*, vol. 66, no. 4, pp. 2061-2068,2015.

[83] B.V. Budaev, A. Ghafari and D.B. Bogy, '"Intense radiative heat transport across a nano-scale gap," *J.Appl.Phys.*, vol. 119, no. 14, pp. 144501,2016.

[84] Y. Ma, A. Ghafari, B.V. Budaev and D.B. Bogy, '"Measurement and simulation of nanoscale gap heat transfer using a read/write head with a contact sensor," *IEEE Trans.Magn.*, vol. 53, no. 2, pp. 1-5,2017.

[85] J. Zheng and D.B. Bogy, '"Numerical simulation of touchdown dynamics of thermal flying-height control sliders," *IEEE Trans.Magn.*, vol. 48, no. 9, pp. 2415-2420,2012.

[86] M. Kurita, J. Xu, M. Tokuyama, S. Saegusa, Y. Maruyama and H. Fukui, '"Simulation of thermal protrusions on magnetic head elements," *JSME International Journal Series C Mechanical Systems, Machine Elements and Manufacturing*, vol. 48, no. 3, pp. 359-362,2005.

[87] M. Kurita, J. Xu, M. Tokuyama, K. Nakamoto, S. Saegusa and Y. Maruyama, '"Flying-height reduction of magnetic-head slider due to thermal protrusion," *IEEE Trans.Magn.*, vol. 41, no. 10, pp. 3007-3009,2005.

[88] L. Huang, B. Stipe, M. Staffaroni, J. Juang, T. Hirano, E. Schreck and F. Huang, '"HAMR thermal modeling including media hot spot," *IEEE Trans.Magn.*, vol. 49, no. 6, pp. 2565-2568,2013.

[89] L. Wu, '"Modelling and simulation of the lubricant depletion process induced by laser heating in heat-assisted magnetic recording system," *Nanotechnology*, vol. 18, no. 21, pp. 215702,2007.

[90] M.S.G. Sarabi and D.B. Bogy, '"Simulation of the Performance of Various PFPE Lubricants Under Heat Assisted Magnetic Recording Conditions," *Tribology Letters*, vol. 56, no. 2, pp. 293-304,2014.

[91] J.B. Dahl and D.B. Bogy, '"Lubricant flow and evaporation model for heat-assisted magnetic recording including functional end-group effects and thin film viscosity," *Tribology Letters*, vol. 52, no. 1, pp. 27-45,2013.

[92] R. Ambekar, V. Gupta and D.B. Bogy, '"Experimental and numerical investigation of dynamic instability in the head disk interface at proximity," *Journal of tribology*, vol. 127, no. 3, pp. 530-536,2005.

[93] M. Honchi, H. Kohira and M. Matsumoto, '"Numerical simulation of slider dynamics during slider–disk contact," *Tribol.Int.*, vol. 36, no. 4-6, pp. 235-240,2003.

[94] A.N. Murthy, B. Feliss, D. Gillis and F.E. Talke, '"Experimental and numerical investigation of shock response in 3.5 and 2.5 in. form factor hard disk drives," *Microsystem technologies*, vol. 12, no. 12, pp. 1109-1116,2006.

[95] R. Rai and D.B. Bogy, '"Parametric study of operational shock in mobile disk drives with disk–ramp contact," *IEEE Trans.Magn.*, vol. 47, no. 7, pp. 1878-1881,2011.

[96] E.M. Jayson, P.W. Smith and F.E. Talke, '"Shock modeling of the head-media interface in an operational hard disk drive," *IEEE Trans.Magn.*, vol. 39, no. 5, pp. 2429-2431,2003.

[97] M.H. Kryder, E.C. Gage, T.W. McDaniel, W.A. Challener, R.E. Rottmayer, G. Ju, Y. Hsia and M.F. Erden, '"Heat assisted magnetic recording," *Proc IEEE*, vol. 96, no. 11, pp. 1810-1835,2008.

[98] D. Li, M. Staffaroni, E. Schreck and B. Stipe, '"A new AFM-based technique to detect the NFT protrusion on HAMR head," *IEEE Trans.Magn.*, vol. 49, no. 7, pp. 3576-3579,2013.

[99] X. Shaomin and D.B. Bogy, '"Flying height modulation for a dual thermal protrusion slider in heat assisted magnetic recording (HAMR)," *IEEE Trans.Magn.*, vol. 49, no. 10, pp. 5222-5226,2013.

[100] T. Rausch, J.D. Trantham, A.S. Chu, H. Dakroub, J.W. Riddering, C.P. Henry, J.D. Kiely, E.C. Gage and J.W. Dykes, '"HAMR drive performance and integration challenges," *IEEE Trans.Magn.*, vol. 49, no. 2, pp. 730-733,2013.

[101] X. Wang, K. Gao, H. Zhou, A. Itagi, M. Seigler and E. Gage, '"HAMR recording limitations and extendibility," *IEEE Trans.Magn.*, vol. 49, no. 2, pp. 686-692,2013.

[102] S. Xiong and D.B. Bogy, '"Investigation of the local temperature increase for heat assisted magnetic recording (HAMR)," *IEEE Trans.Magn.*, vol. 50, no. 4, pp. 1-6,2014.